General theory of optical reflection from a thin film on a solid and its application to heteroepitaxy

X. D. Zhu*

Department of Physics, University of California, Davis, California 95616, USA

Y. Y. Fei, X. Wang, H. B. Lu, and G. Z. Yang

Beijing National Laboratory for Condensed Matter Physics, Institute of Physics, Chinese Academy of Sciences, Beijing 100080, China

Light reflection from an optically smooth yet atomically rough film on a smooth solid substrate formed by deposition or erosion is a convenient source of information on morphology and chemical makeup of the film. We show that changes in optical reflectivity for *s*-polarized (TE mode) and *p*-polarized (TM mode) components, defined as $(r_p - r_{p0})/r_{p0} - (r_s - r_{s0})/r_{s0} \equiv \Delta_p - \Delta_s$ induced by such a film, are generally related to structural and chemical properties of such a film through a mean-field theory. Here, r_{p0} and r_{s0} are the reflectivities of the substrate, and r_p and r_s are the reflectivities when the film is added. According to the theory, $\Delta_p - \Delta_s$ consists of a term that is proportional to the thickness of the rough portion of the film, a term that is proportional to the density of unit cells embedded in terraces, and a term that is proportional to the density of unit cells situated at step edges. The proportionality constants are functions of the overall thickness and chemical makeup of the film. We apply the theory to the analysis of a wide range of growth and adsorption experiments studied with the oblique-incidence reflectivity difference technique.

I. INTRODUCTION

Homoepitaxy and heteroepitaxy of materials are main fabrication methods for producing novel materials and material forms. Monitoring *in situ* the morphology and chemical makeup of as-grown materials is crucial to characterization and control of the quality and efficacy of these processes.[1–16] Being nonintrusive and compatible with a wide range of growth or removal conditions (volatile or otherwise), optical reflection from material surfaces has been widely used to follow growth, erosion, and other surface-bound processes. Since the optical response from a surface is sensitive to both crystallinity and chemical makeup, this dual sensitivity can be exploited in investigation of growth and surface-bound reactions. McGilp,[10] Aspnes and co-workers,[11–13] Blackmann *et al.*,[14] and Zhu and co-workers[15–22] have studied a wide range of kinetic processes on solids in vacuum and in electrochemical environment.

Because an optical wavelength (λ) is much larger than the size of an atom, light reflection from a thin film on a solid substrate contains structural and chemical information of the film through "averaged" optical dielectric responses. This raises the following questions: (1) How much detail can one learn from optical reflection off a growth surface? (2) How does the optical response change as the film thickness d increases beyond the limit of $d/\lambda \ll 1$? These are the topics of this paper.

In an earlier paper, Zhu proposed a mean-field model for dealing with optical reflection from an atomically rough film with characteristic length scales such as the root-mean-square roughness and the average thickness much less than an optical wavelength.[23] He computed the sum of reflection from terraces on the surface of the film, each of which consisting of terrace atoms and step edge atoms (characterized by their respective optical dielectric constants), an optically thin layer of bulk-phase atoms that may be different from the

substrate, and the substrate. The main finding was that *the optical reflectivity difference has a term that is proportional to the mean thickness of the film and a term that varies linearly with the density of atoms at step edges.* The model was limited to optically thin films and to crystalline materials with one atom per unit cell. In this paper, we generalize the model that allows the thickness of the bulk-phase layer of a film to be optically thick. We further generalize the model that covers more complex materials such as oxides with unit cells containing more than one atomic constituent. As a result, chemical makeups of unit cells may be different and even evolving in time, depending on whether they are on terraces, at step edges, or inside the bulk-phase layer of the film.

II. GENERAL THEORY OF OPTICAL REFLECTION FROM AN ATOMICALLY ROUGH FILM ON A SMOOTH SOLID SUBSTRATE

In Fig. 1, we show a sketch of an atomically rough film on a smooth solid substrate (ε_s). The film consists of a smooth part with a thickness d_{init} that can be *optically thick* and a rough part with an average thickness $d_{\text{rough}} \equiv \langle d \rangle - d_{\text{init}}$ that is optically thin ($d_{\text{rough}}/\lambda \ll 1$). The top of the film is in contact with a transparent ambient with optical dielectric constant ε_0. The unit cells inside the film are characterized by a bulk-phase optical dielectric constant $\varepsilon_{d,\text{bulk}}$. The unit cells embedded in the terraces are characterized by an optical dielectric constant $\varepsilon_{d,\text{terr}}$. The unit cells situated at step edges are characterized by an effective dielectric constant $\varepsilon_{d,\text{step}}$. As noted by Zhu earlier,[23] the contribution to the optical reflection from a terrace can be separated into a part from the terrace-bound unit cells and a part from the step-edge-bound unit cells. $\varepsilon_{d,\text{step}}$ generally differs from $\varepsilon_{d,\text{terr}}$, in part because the effective electric field experienced by the unit cells at step edges is different and somewhat ill defined. As done by Zhu,
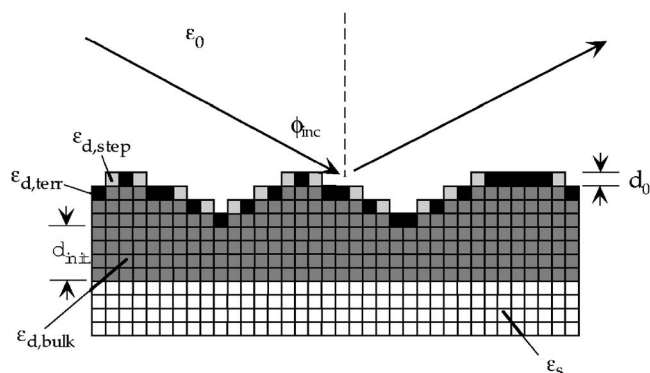
FIG. 1. Sketch of a crystalline film on top of a smooth substrate (white squares, characterized by ε_s). Dark gray squares: atoms inside the film, characterized by $\varepsilon_{d,\text{bulk}}$. Black squares: terrace atoms, characterized by $\varepsilon_{d,\text{terr}}$. Light gray squares: step edge atoms, characterized by an effective $\varepsilon_{d,\text{step}}$. The smooth portion of the film has a thickness d_{init} that can be optically thick. The film is illuminated with a collimated, monochromatic light beam from the ambient with ε_0 at an incidence angle ϕ_{inc}.

we treat this electric field in a mean-field sense and incorporate the unaccounted effect into $\varepsilon_{d,\text{step}}$.

Let a collimated beam of light at wavelength λ be incident at angle ϕ_{inc} from the ambient onto the film as illustrated in Fig. 1. We treat the radiation from terraces at the same height from the substrate surface *collectively* by having these terrace segments "coalesce" into one large terrace and further separating it into a region with $\varepsilon_{d,\text{terr}}$ and a region with $\varepsilon_{d,\text{step}}$, as shown in Fig. 2.

Let θ_j $(j \geq 0)$ be the coverage of the jth coalesced terrace at a distance (height) $d_j = jd_0 + d_{\text{init}} \equiv \delta d_j + d_{\text{init}}$ away from the substrate surface. d_0 is the unit-cell thickness. Let $\theta_{j,t}$ be the coverage of terrace-bound unit cells and $\theta_{j,\text{step}}$ be the coverage of step-edge-bound unit cells so that $\theta_j = \theta_{j,t} + \theta_{j,\text{step}}$. We should note that $\theta_{0,\text{step}} = 0$ and $\theta_0 = \theta_{0,t}$. Furthermore, when $d_{\text{init}} = 0$, the optical dielectric constant of the 0th terrace is that of the substrate $\varepsilon_{s,\text{terr}}$ rather than $\varepsilon_{d,\text{terr}}$. This distinction is
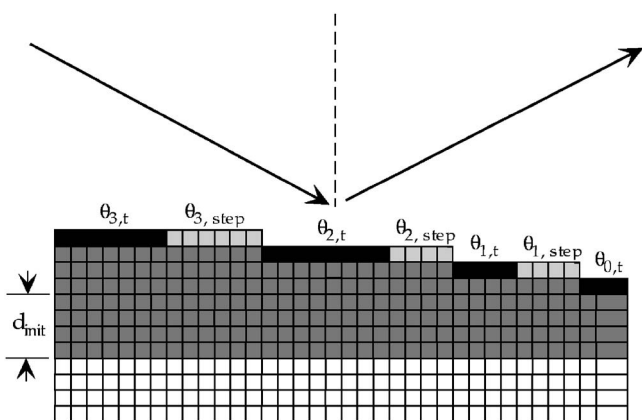
FIG. 2. Sketch of the rearrangement of the crystalline film (as displayed in Fig. 1) by grouping terrace-bound unit cells and step-edge-bound unit cells into connected terraces according to the distance from the substrate surface for the purpose of computing specular light reflection.

useful when one studies adsorption and desorption of submonolayer adsorbates on a solid substrate. In general, we have

$$\theta_0 + \sum_{j=1} \theta_j = \theta_0 + \sum_{j=1} \theta_{j,t} + \sum_{j=1} \theta_{j,\text{step}} = \theta_0 + \theta_t + \theta_{\text{step}} = 1.$$
(1)

Here, we define the total coverage of terrace-bound unit cells as $\theta_t \equiv \sum_{j=1} \theta_{j,t}$ and the total coverage of step-edge-bound unit cells as $\theta_{\text{step}} \equiv \sum_{j=1} \theta_{j,\text{step}}$.

The reflectivity for s-polarized and p-polarized light from the film is the sum of contributions from all terraces,

$$r_s = \sum_{j=1} r_s^{(\text{step})}(d_j) \theta_{j,\text{step}} \exp(-i4\pi \delta d_j \cos \phi_{\text{inc}}/\lambda)$$
$$+ \sum_{j=1} r_s^{(\text{terr})}(d_j) \theta_{j,t} \exp(-i4\pi \delta d_j \cos \phi_{\text{inc}}/\lambda) + r_s(d_{\text{init}})\theta_0,$$
(2a)

$$r_p = \sum_{j=1} r_p^{(\text{step})}(d_j) \theta_{j,\text{step}} \exp(-i4\pi \delta d_j \cos \phi_{\text{inc}}/\lambda)$$
$$+ \sum_{j=1} r_p^{(\text{terr})}(d_j) \theta_{j,t} \exp(-i4\pi \delta d_j \cos \phi_{\text{inc}}/\lambda) + r_p(d_{\text{init}})\theta_0.$$
(2b)

$r_s^{(\text{terr})}(d_j)$ and $r_p^{(\text{terr})}(d_j)$ are the reflectivities for s and p-polarized components from a four-layer system that consists of the ambient, a monolayer of terrace-bound unit cells, a layer of bulk-phase film with a thickness of d_j, and the substrate. $r_s^{(\text{step})}(d_j)$ and $r_p^{(\text{step})}(d_j)$ are the reflectivities from a similar four-layer system in which the monolayer of terrace-bound unit cells is replaced by a monolayer of step-edge-bound unit cells. $r_s(d_{\text{init}})$ and $r_p(d_{\text{init}})$ are the reflectivities from a three-layer system consisting of the ambient, a layer of bulk-phase film with a thickness of d_{init}, and the substrate. The mean thickness of the rough part of the film is given by $d_{\text{rough}} = \sum_{j=1} \delta d_j \theta_j$. We assume that δd_j is small compared to optical wavelengths. As a result, the corrections due to the rough part of the film to $r_s(d_{\text{init}})$ and $r_p(d_{\text{init}})$ are in the order of d_{rough}/λ, and thus small. We rewrite $r_s^{(\text{terr})}(d_j)$, $r_p^{(\text{terr})}(d_j)$, $r_s^{(\text{step})}(d_j)$, and $r_p^{(\text{step})}(d_j)$ in terms of $r_s(d_{\text{init}})$ and $r_p(d_{\text{init}})$,

$$r_s^{(\text{terr})}(d_j) = r_s(d_{\text{init}})[1 + \Delta_s^{(\text{bulk})}(d_{\text{init}}, \delta d_j) + \Delta_s^{(\text{terr})}(d_{\text{init}}, d_0)],$$
(3a)

$$r_p^{(\text{terr})}(d_j) = r_p(d_{\text{init}})[1 + \Delta_p^{(\text{bulk})}(d_{\text{init}}, \delta d_j) + \Delta_p^{(\text{terr})}(d_{\text{init}}, d_0)],$$
(3b)

$$r_s^{(\text{step})}(d_j) = r_s(d_{\text{init}})[1 + \Delta_s^{(\text{bulk})}(d_{\text{init}}, \delta d_j) + \Delta_s^{(\text{step})}(d_{\text{init}}, d_0)],$$
(4a)

$$r_p^{(\text{step})}(d_j) = r_p(d_{\text{init}})[1 + \Delta_p^{(\text{bulk})}(d_{\text{init}}, \delta d_j) + \Delta_p^{(\text{step})}(d_{\text{init}}, d_0)].$$
(4b)

Inserting Eqs. (3) and (4) into Eq. (2) and keeping only terms up to ones that vary linearly with δd_j,

$$r_s = r_s(d_{\text{init}}) \left\{ (1 - \theta_0) + (-i4\pi d_{\text{rough}} \cos \phi_{\text{inc}}/\lambda) \right.$$

$$+ \sum_{j=1} \theta_j \Delta_s^{(\text{bulk})}(d_{\text{init}}, \delta d_j) + \Delta_s^{(\text{terr})}(d_{\text{init}}, d_0)(1 - \theta_0 - \theta_{\text{step}})$$

$$\left. + [\Delta_s^{(\text{step})}(d_{\text{init}}, d_0) - \Delta_s^{(\text{terr})}(d_{\text{init}}, d_0)]\theta_{\text{step}} \right\}, \quad (5a)$$

$$r_p = r_p(d_{\text{init}}) \left\{ (1 - \theta_0) + (-i4\pi d_{\text{rough}} \cos \phi_{\text{inc}}/\lambda) \right.$$

$$+ \sum_{j=1} \theta_j \Delta_p^{(\text{bulk})}(d_{\text{init}}, \delta d_j) + \Delta_p^{(\text{terr})}(d_{\text{init}}, d_0)(1 - \theta_0 - \theta_{\text{step}})$$

$$\left. + [\Delta_p^{(\text{step})}(d_{\text{init}}, d_0) - \Delta_p^{(\text{terr})}(d_{\text{init}}, d_0)]\theta_{\text{step}} \right\}. \quad (5b)$$

We define the *net* optical reflectivity difference as

$$\Delta_p - \Delta_s \equiv \frac{r_p - r_p(d_{\text{init}})}{r_p(d_{\text{init}})} - \frac{r_s - r_s(d_{\text{init}})}{r_s(d_{\text{init}})}. \quad (6)$$

From Eq. (6), we arrive at

$$\Delta_p - \Delta_s = \sum_{j=1} [\Delta_p^{(\text{bulk})}(d_{\text{init}}, \delta d_j) - \Delta_s^{(\text{bulk})}(d_{\text{init}}, \delta d_j)]\theta_j$$

$$+ [\Delta_p^{(\text{terr})}(d_{\text{init}}, d_0) - \Delta_s^{(\text{terr})}(d_{\text{init}}, d_0)](1 - \theta_0 - \theta_{\text{step}})$$

$$+ [\Delta_p^{(\text{step})}(d_{\text{init}}, d_0) - \Delta_s^{(\text{step})}(d_{\text{init}}, d_0)]\theta_{\text{step}}. \quad (7)$$

From the multilayer thin-film optics and after some algebraic rearrangement (see Appendix A), we cast the coefficients in Eq. (7) into the same form as in Ref. 23,

$$\Delta_p^{(\text{terr})}(d_{\text{init}}, d_0) - \Delta_s^{(\text{terr})}(d_{\text{init}}, d_0)$$

$$= \alpha_{\text{eff}}(d_{\text{init}}) \left[\frac{(\varepsilon_{d,\text{terr}} - \varepsilon_0)[\varepsilon_{d,\text{terr}} - \varepsilon_{s,\text{eff}}(d_{\text{init}})]}{\varepsilon_{d,\text{terr}}} \right] d_0, \quad (8)$$

$$\Delta_p^{(\text{step})}(d_{\text{init}}, d_0) - \Delta_s^{(\text{step})}(d_{\text{init}}, d_0)$$

$$= \alpha_{\text{eff}}(d_{\text{init}}) \left[\frac{(\varepsilon_{d,\text{step}} - \varepsilon_0)[\varepsilon_{d,\text{step}} - \varepsilon_{s,\text{eff}}(d_{\text{init}})]}{\varepsilon_{d,\text{step}}} \right] d_0, \quad (9)$$

$$\Delta_p^{(\text{bulk})}(d_{\text{init}}, \delta d_j) - \Delta_s^{(\text{bulk})}(d_{\text{init}}, \delta d_j)$$

$$= \alpha_{\text{eff}}(d_{\text{init}}) \left[\frac{(\varepsilon_{d,\text{bulk}} - \varepsilon_0)[\varepsilon_{d,\text{bulk}} - \varepsilon_{s,\text{eff}}(d_{\text{init}})]}{\varepsilon_{d,\text{bulk}}} \right] \delta d_j. \quad (10)$$

The two new parameters in these equations are defined as $\alpha_{\text{eff}}(d_{\text{init}}) \equiv \alpha(\varepsilon_0; \varepsilon_{d,\text{bulk}}, d_{\text{init}}; \varepsilon_s)$ and $\varepsilon_{s,\text{eff}}(d_{\text{init}}) \equiv \varepsilon_s(\varepsilon_0; \varepsilon_{d,\text{bulk}}, d_{\text{init}}; \varepsilon_s)$. In Appendix A, we present a brief derivation of Eqs. (8)–(10) and the full expressions for $\alpha(\varepsilon_0; \varepsilon_{d,\text{bulk}}, d_{\text{init}}; \varepsilon_s)$ and $\varepsilon_s(\varepsilon_0; \varepsilon_{d,\text{bulk}}, d_{\text{init}}; \varepsilon_s)$. When $d_{\text{init}} = 0$, $\varepsilon_{s,\text{eff}}(d_{\text{init}} = 0) = \varepsilon_s$, and $\alpha_{\text{eff}}(d_{\text{init}})$ is reduced to that of Eq. (10) in Ref. 23,

$$\alpha_{\text{eff}}(d_{\text{init}} = 0) = \alpha = (-i)\frac{4\pi \cos \phi_{\text{inc}} \sin^2 \phi_{\text{inc}} \sqrt{\varepsilon_0}\varepsilon_s}{\lambda(\varepsilon_s - \varepsilon_0)(\varepsilon_s \cos^2 \phi_{\text{inc}} - \varepsilon_0 \sin^2 \phi_{\text{inc}})}. \quad (11)$$

We now write Eq. (7) into a general form after inserting Eqs. (8)–(10),

$$\Delta_p - \Delta_s = \alpha_{\text{eff}}(d_{\text{init}}) \left[\frac{(\varepsilon_{d,\text{bulk}} - \varepsilon_0)[\varepsilon_{d,\text{bulk}} - \varepsilon_{s,\text{eff}}(d_{\text{init}})]d_{\text{rough}}}{\varepsilon_{d,\text{bulk}}} \right.$$

$$+ \frac{(\varepsilon_{d,\text{terr}} - \varepsilon_0)[\varepsilon_{d,\text{terr}} - \varepsilon_{s,\text{eff}}(d_{\text{init}})]d_0}{\varepsilon_{d,\text{terr}}}(1 - \theta_0 - \theta_{\text{step}})$$

$$\left. + \frac{(\varepsilon_{d,\text{step}} - \varepsilon_0)[\varepsilon_{d,\text{step}} - \varepsilon_{s,\text{eff}}(d_{\text{init}})]d_0}{\varepsilon_{d,\text{step}}}\theta_{\text{step}} \right]. \quad (12)$$

Equation (12) is the main result of this paper. For an arbitrary d_{init}, the oblique-incidence reflectivity difference (OI-RD) signal *again* consists of three terms: one that is proportional to the mean thickness of the rough part of the film $d_{\text{rough}} = \langle d \rangle - d_{\text{init}}$, one that is proportional to the coverage of terrace-bound unit cells $1 - \theta_0 \approx \theta_t$, and one that is proportional to the coverage of step-edge-bound unit cells θ_{step}. $\varepsilon_{s,\text{eff}}(d_{\text{init}})$ (see Appendix A) is generally oscillatory with increasing d_{init} and can in turn cause the terms in Eq. (12) to change signs during growth.

In the next section, we apply Eq. (12) to analyze the optical response to changes in surface morphology and chemical makeup during adsorption, desorption, and epitaxy on a solid substrate in various cases. For example, θ_{step} varies with the total amount of deposited material in a tractable way as determined by the kinetics of growth. In a perfect layer-by-layer growth (characterized by a sequence of nucleation, growth, and coalescence in one monolayer before the same sequence repeats for the next monolayer), $\theta_{\text{step}} \sim (\sqrt{N_n/N_s})\theta_0(1 - \theta_0)$.[24] When $1 - \theta_0$ increases from 0 up to 1, θ_{step} goes through an oscillation that peaks at $1 - \theta_0 = 0.5$. In a quasi-layer-by-layer growth, at the completion of a monolayer-worth deposition, the deposited unit cells are distributed in more than one terrace. If the deposition continues, θ_{step} still oscillates but with a reduced or even diminishing amplitude.[16] The details depend on the growth kinetics as we will show toward the end of the next section. In a multilayer or three-dimensional growth, θ_{step} increases monotonically with the total deposited materials.[18] Measurements of $\Delta_p - \Delta_s$ (the OI-RD signals) allow one to study kinetics of growth and to extract a surprising amount of quantitative information. The advantages of such an optical technique over conventional electron, thermal atom, and/or x-ray beam techniques[1–5] are its versatility in implementation, its applicability to environments inaccessible to mass particles, and its sensitivity to chemical makeup of a deposited thin film.

III. ADSORPTION AND GROWTH OF THIN FILMS STUDIED WITH OI-RD MEASUREMENTS

A. Adsorption and desorption of submonolayers on single-crystal metals

Using the OI-RD technique, Zhu and co-workers have performed a series of studies of adsorption and desorption of monolayer adsorbates on Ni, Cu, and Nb in ultrahigh vacuum[15,17,18,25,26] and of electrodeposition and dissolution of metallic monolayers on polycrystalline substrates of Au

and Cu in electrochemical cells.[22,27,28] In these cases, d_{init} $=0$. In addition, the first term in Eq. (12) is absent, and the second term dominates the third term. The OI-RD signals are proportional to the coverage of adsorbates, $\theta = 1 - \theta_0$,

$$\Delta_p - \Delta_s \approx \frac{\alpha d_0 (\varepsilon_d - \varepsilon_0)(\varepsilon_d - \varepsilon_s)}{\varepsilon_d} \theta. \quad (13)$$

Equation (13) has been used to analyze kinetics of adsorption and desorption of adsorbates on metals in ultrahigh vacuum. When two types of adsorbates coadsorb on a solid surface, characterized with distinct optical dielectric constants ($\varepsilon_d^{(1)}$ and $\varepsilon_d^{(2)}$) and coverages ($\theta^{(1)}$ and $\theta^{(2)}$), Eq. (13) can be generalized to the following useful form:

$$\Delta_p - \Delta_s \approx \alpha d_0 \left[\frac{(\varepsilon_d^{(1)} - \varepsilon_0)(\varepsilon_d^{(1)} - \varepsilon_s)}{\varepsilon_d^{(1)}} \theta^{(1)} \right.$$
$$\left. + \frac{(\varepsilon_d^{(2)} - \varepsilon_0)(\varepsilon_d^{(2)} - \varepsilon_s)}{\varepsilon_d^{(2)}} \theta^{(2)} \right], \quad (14)$$

provided that the effect of the interaction between two types of adsorbates on $\varepsilon_d^{(1)}$ and $\varepsilon_d^{(2)}$ can be neglected. As long as the coefficients in front of $\theta^{(1)}$ and $\theta^{(2)}$ are not in phase, Eq. (14) can be used to monitor coverages of two adsorbates from the measurement of the real and imaginary parts of $\Delta_p - \Delta_s$, after an initial calibration. For example, Zhu and co-workers studied coadsorption as well as separate adsorption of Xe and hydrogen atoms on Cu(111).[25,26] They found that the optical dielectric constant of adsorbed Xe adatoms $\varepsilon_d^{(Xe)}$ is essentially the same as that of a bulk-phase Xe. At the incidence angle $\phi_{inc} = 67°$, these authors found that up to a full monolayer, the adsorption of Xe on Cu(111) only induces a change in $\text{Im}\{\Delta_p - \Delta_s\}$ such that

$$(\Delta_p - \Delta_s)|_{Xe} \approx (a_{Xe} + ib_{Xe})\theta^{(Xe)} = i0.0065\theta^{(Xe)},$$
$$(14a)$$

i.e., $a_{Xe} = 0$ and $b_{Xe} = 0.0065$. At the same incidence angle, the separate adsorption of hydrogen atoms on Cu(111), on the other hand, has an effective optical constant $\varepsilon_d^{(H)}$ such that it induces a large change in $\text{Re}\{\Delta_p - \Delta_s\}$ and a relative small one in $\text{Im}\{\Delta_p - \Delta_s\}$,

$$(\Delta_p - \Delta_s)|_H \approx (a_H + ib_H)\theta^{(H)} = (-0.0057 - i0.0017)\theta^{(H)},$$
$$(14b)$$

i.e., $a_H = -0.0057$ and $b_H = -0.0017$. When Xe and hydrogen adatoms are both present on Cu(111), the coverage of hydrogen atoms and that of Xe atoms can be determined from simultaneously measured $\text{Re}\{\Delta_p - \Delta_s\}$ and $\text{Im}\{\Delta_p - \Delta_s\}$ under the same optical detection condition. In this case, Eq. (14) can be written as

$$\Delta_p - \Delta_s \approx (a_H + ib_H)\theta^{(H)} + (a_{Xe} + ib_{Xe})\theta^{(Xe)}. \quad (14c)$$

From the $\Delta_p - \Delta_s$ measured under coadsorption condition, the respective coverages of hydrogen adatoms and Xe adatoms are determined by solving Eq. (14c) for $\theta^{(H)}$ and $\theta^{(Xe)}$.

In Fig. 3, we display $\Delta_p - \Delta_s$ (with properly determined signs) from Cu(111) measured as a function of time in a sequence of Xe and hydrogen adsorption and desorption pro-
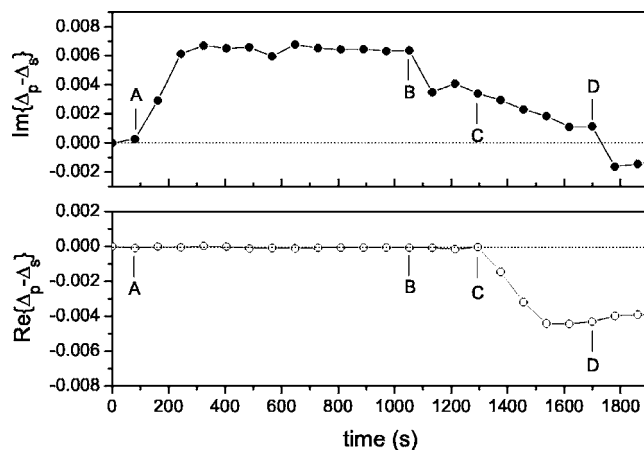
FIG. 3. Real and imaginary parts of $\Delta_p - \Delta_s$ from Cu(111) in ultrahigh vacuum in response to a sequence of adsorption, coadsorption, and desorption of Xe and hydrogen atoms at the substrate temperature $T = 38$ K. At point A, Cu(111) is exposed to Xe gas until a full monolayer of Xe is formed. At point B, the Xe-covered Cu is irradiated with the interference pattern (formed with dual-beam nanosecond optical pulses at 0.532 μm) that thermally removes some or all of the Xe adatoms from the region of bright interference fringes and in turn exposes the bare Cu surface (Ref. 26). At point C, the Cu surface (now partially covered with Xe) is exposed to hot hydrogen molecules that become dissociated and adsorbed on the exposed part of the surface. At point D, the Cu surface with coadsorbed Xe and hydrogen is irradiated with single-beam nanosecond optical pulses at 0.532 μm that *uniformly* remove the remaining Xe adatoms while leaving hydrogen adatoms untouched.

cesses: (A) At $t = 80$ s, a clean Cu(111) at 38 K is exposed to Xe gas for $\sim$200 s so that it is covered by a full monolayer of Xe adatoms. (B) At $t = 1060$ s, the Xe-covered Cu(111) is irradiated once with a spatially overlapping, temporally coherent pair of optical pulses at 0.532 μm that form an interference pattern with a periodicity of 5.45 μm, and the interference pattern thermally desorbs Xe adatoms in regions of bright fringes while leaving Xe adatoms unchanged in regions of dark fringes. (C) At $t = 1290$ s, the Cu(111) surface partially covered by the remaining Xe adatoms is exposed to hot hydrogen molecules that dissociatively adsorb on the uncovered part of Cu(111). (D) At $t = 1700$ s, the Cu(111) surface covered with coadsorbed Xe and hydrogen adatoms is irradiated with single optical pulses at 0.532 μm so that the remaining Xe is thermally desorbed or "erased," leaving behind only the hydrogen adatoms [due to a much stronger binding of hydrogen atom to Cu(111)]. In Fig. 4, we display the coverage of Xe adatoms and of hydrogen adatoms on Cu(111) (during the same sequence of events) determined from Eq. (14c) and the data shown in Fig. 3, with $\theta^{(H)}$ $= \text{Re}\{\Delta_p - \Delta_s\}/a_H$ and $\theta^{(Xe)} = (\text{Im}\{\Delta_p - \Delta_s\} - b_H\theta^{(H)})/b_{Xe}$.

This feature of the OI-RD technique makes it advantageous over the work-function technique for determination of coverage of adsorbates as the latter cannot determine coverages of two coadsorbed species from only one measurable quantity.
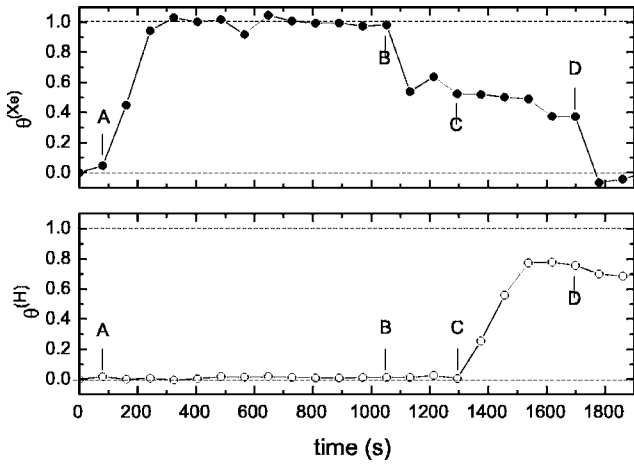
FIG. 4. Coverages of coadsorbed Xe ($\theta^{(Xe)}$) and hydrogen atoms ($\theta^{(H)}$) on Cu(111) during the sequence of adsorption, coadsorption, and desorption as described in Fig. 3. $\theta^{(Xe)}$ and $\theta^{(H)}$ are computed from the experimental values of $\Delta_p - \Delta_s$ as displayed in Fig. 3 using $\theta^{(H)} = \text{Re}\{\Delta_p - \Delta_s\}/a_H$ and $\theta^{(Xe)} = (\text{Im}\{\Delta_p - \Delta_s\} - b_H \theta^{(H)})/b_{Xe}$ (see the main text).

B. Electrodeposition of Pb films on Cu(100)

Gray and co-workers studied electrodeposition of Co monolayers on polycrystalline Au and of Pb multilayers on (100)-terminated polycrystalline Cu using the OI-RD technique as the *in situ* probe.[22,27,28]

At electric potentials less negative than the equilibrium potential for bulk-phase Pb formation, underpotential deposited (UPD) Pb form a *sub*monolayer film on Cu(100). The Pb coverage depends on how close the potential is to the equilibrium value for bulk-phase Pb formation. These authors found that the OI-RD signal in this UPD regime is described well with Eq. (13) and the proportionality constant in front of $\theta = 1 - \theta_0$ or equivalently $\varepsilon_d^{(Pb)}$ can be determined experimentally from the dissolution of the UPD Pb.

At electric potentials more negative than the equilibrium potential, overpotential deposited Pb form a "bulk-phase" film on the UPD-Pb-monolayer-covered Cu(100). Due to the large disparity in surface tension between Pb and Cu, the Pb film consists of three-dimensional islands (Volmer-Weber growth mode). When the electric potential is far from the equilibrium value (i.e., high overpotential), the density of nucleation centers is high so that the average island-island distance is small and the deposited Pb forms a granular film with a mean thickness d_{rough} that fully covers the Cu surface. The optical response from the Pb film is dominated by the first term in Eq. (12),

$$\Delta_p - \Delta_s = \frac{\alpha(\varepsilon_d^{(Pb)} - \varepsilon_0^{(water)})(\varepsilon_d^{(Pb)} - \varepsilon_s^{(Cu)})d_{rough}}{\varepsilon_d^{(Pb)}}. \quad (15)$$

Equation (15) provides a good description to the observation of Gray *et al.*[28] In Fig. 5, we show the real and imaginary parts of the OI-RD signal measured from a polycrystalline Cu(100) surface (the working electrode) during a continuous deposition of Pb at the potential of −0.625 V referenced to a saturated calomel reference electrode (SCE) in an aqueous
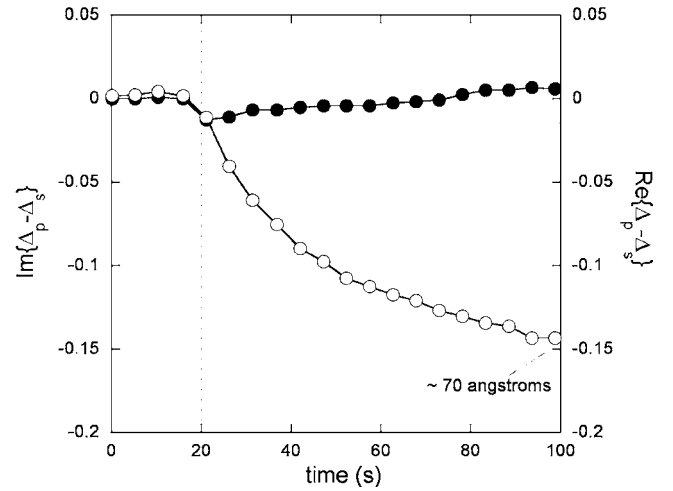
FIG. 5. Experimentally measured real and imaginary parts of $\Delta_p - \Delta_s$ from a polycrystalline Cu(100) (as the working electrode) in an electrochemical cell in response to overpotential deposition of Pb from an aqueous solution of 10 mM HCl+1 mM Pb(ClO$_4$)$_2$. At $t = 16$ s, the potential of the Cu(100) surface is stepped from a holding value of −0.2 V (SCE) to −0.625 V (SCE). The equilibrium potential for bulk-phase Pb deposition is $E_{Pb/Pb^{2+}} = -0.52$ V (SCE). At $t = 20$ s, the first Pb monolayer (the underpotential deposition layer) is formed and the growth of a bulk-phase granular Pb film commences. The Pb deposition rate is ∼0.3 ML/s. The spacing between two neighboring (111) planes of bulk-phase Pb is 2.85 Å. After 80 s, the net deposited Pb is roughly $d_{rough} = 70$ Å.

solution of 10 mM HCl+1 mM Pb(ClO$_4$)$_2$. At $t = 16$ s, the potential is suddenly switched from a holding value of −0.2 V (at which there is neither deposition from the solution nor dissolution from the Cu electrode) to $E_{dep} = -0.625$ V (at which the electrodeposition of bulk-phase Pb on the Cu electrode takes place). The pH of the electrolyte is 2.25. Both Re$\{\Delta_p - \Delta_s\}$ (open circles) and Im$\{\Delta_p - \Delta_s\}$ (solid circles) decrease initially until the first monolayer of Pb is formed on the Cu surface. This first layer is the UPD layer as it can form at the potential less in magnitude than the equilibrium potential $E_{Pb/Pb^{2+}} = -0.52$ V (SCE) for bulk-phase Pb formation. On top of the first Pb monolayer (the UPD layer), a granular film of Pb grows. The corresponding Re$\{\Delta_p - \Delta_s\}$ continues to decrease, while Im$\{\Delta_p - \Delta_s\}$ increases but with a smaller rate. In Fig. 6, we display the calculated $\Delta_p - \Delta_s$ from a Cu surface vs the thickness of smooth Pb overlayer. The good agreement between Figs. 5 and 6 shows that Eq. (15) indeed provides an adequate description of a thin granular film on a "smooth" substrate.

When the electric potential is close to the equilibrium potential (i.e., low overpotential), the density of the nucleation is small so that the deposited Pb forms large islands with the island-island distance larger than the mean diameter of the Pb islands. As a result, the UPD-Pb-covered Cu surface is mostly free of overpotential deposited Pb except for a few large Pb crystallites. The optical response, particularly Re$\{\Delta_p - \Delta_s\}$ from such a surface is dramatically different from the prediction of Eq. (15) and is complicated by the large light scattering off specular direction from these large Pb crystallites.
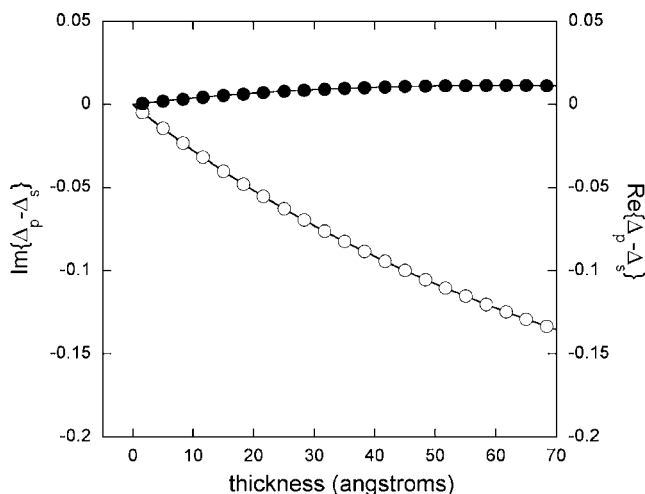
FIG. 6. Calculated $\Delta_p - \Delta_s$ from a smooth film of bulk-phase Pb on a smooth Cu surface vs film thickness d using Eq. (15) and the published optical dielectric constants of bulk-phase Pb, Cu, and water, $\varepsilon_s^{(Cu)} = -10.4 + i1.76$, $\varepsilon_d^{(Pb)} = -7.6 + i13.5$, and $\varepsilon_0^{(water)} = 1.77$. This figure is in good agreement with Fig. 5 during the growth of bulk-phase Pb, indicating that even for a rough film such as a granular Pb film on Cu(100), the predominant contribution to $\Delta_p - \Delta_s$ is indeed given by Eq. (15).

C. Rare-gas growth on single crystal metals

Zhu and co-workers studied the growth of xenon on Ni(111) and Nb(110) in ultrahigh vacuum using a combination of low-energy electron-diffraction and OI-RD techniques.[15,17,18] Because Ni(111) is a lattice- and symmetry-matched substrate while Nb(110) is a mismatched one for a Xe film that prefers to be (111) terminated, these studies offered the opportunity to examine the effect of substrate lattice on growth mode and morphology of rare-gas films. The optical dielectric constant of Xe atoms embedded in the Xe terraces is roughly the same as that of bulk-phase Xe, $\varepsilon_{d,\mathrm{terr}}^{(Xe)} = \varepsilon_{d,\mathrm{bulk}}^{(Xe)}$. The effective optical dielectric constant of Xe atoms situated at step edges $\varepsilon_{d,\mathrm{step}}^{(Xe)}$ includes the effect of the local electric field and is different from $\varepsilon_{d,\mathrm{bulk}}^{(Xe)}$. In these studies, the largest thickness of Xe films is still much smaller than optical wavelengths. Consequently, Eq. (12) is specialized into the following form ($\varepsilon_0 = 1$):

$$\Delta_p - \Delta_s = \alpha \left\{ \frac{(\varepsilon_{d,\mathrm{bulk}}^{(Xe)} - 1)(\varepsilon_{d,\mathrm{bulk}}^{(Xe)} - \varepsilon_s)\langle d \rangle}{\varepsilon_{d,\mathrm{bulk}}^{(Xe)}} \right.$$
$$+ \frac{(\varepsilon_{d,\mathrm{terr}}^{(Xe)} - 1)(\varepsilon_{d,\mathrm{terr}}^{(Xe)} - \varepsilon_s)d_0}{\varepsilon_{d,\mathrm{terr}}^{(Xe)}}(1 - \theta_0)$$
$$+ \left. \left[\frac{(\varepsilon_{d,\mathrm{step}}^{(Xe)} - \varepsilon_{d,\mathrm{terr}}^{(Xe)})(\varepsilon_{d,\mathrm{step}}^{(Xe)} \varepsilon_{d,\mathrm{terr}}^{(Xe)} - \varepsilon_s)d_0}{\varepsilon_{d,\mathrm{step}}^{(Xe)} \varepsilon_{d,\mathrm{terr}}^{(Xe)}} \right] \theta_{\mathrm{step}} \right\}.$$
(16)

The first two terms increase with the mean thickness $\langle d \rangle$ of deposited Xe that includes both the smooth and the rough portions of the film. The third term is noticeable in the experiments of Nabighian *et al.*[18] and Thomas *et al.*,[15] signified by an oscillatory component on top of the envelope of Δ_p

$-\Delta_s$ when the growth of Xe on Ni(111) and Nb(110) is performed at around 40 K. The oscillation period corresponds to deposition of a full Xe monolayer. This indicates that the oscillation comes from the change in the step density and is characteristic of a layer-by-layer growth. As derived in Appendix B, we can relate the coverage of step-edge-bound Xe adatoms to the roughness Δ^2 of the Xe film by[24]

$$\theta_s \cong 2\sqrt{N_n/N_s}\sqrt{\Delta^2}.$$
(17)

The roughness is defined by the well-known relation[29]

$$\Delta^2 = \sum_{j=0} (j - Rt)^2 \theta_j.$$
(18)

N_n is the saturation density of stable two-dimensional Xe islands on the growth surface.[30] When the nucleation takes place predominantly at impurity or defect sites, N_n can be quite large. N_s is the surface number density of Xe adatoms at the full monolayer. R is the deposition rate in unit of the number of deposited Xe monolayers per unit time. For a perfect layer-by-layer growth, $\theta_0 = 1 - Rt$, $\theta_1 = Rt$, and $\theta_{j>1} = 0$. Consequently, $\theta_s \cong 2\sqrt{N_n/N_s}\sqrt{(1 - Rt)Rt}$ varies periodically with a time period being the time to deposit one monolayer. θ_s peaks to $\theta_{s,\mathrm{MAX}} \cong (\sqrt{N_n/N_s})/2$. Nabighian *et al.* observed that the oscillation amplitude in $\Delta_p - \Delta_s$ in response to Xe growth on Ni(111) was quite large.[18] They attributed the observation to a nearly perfect layer-by-layer growth that was dominated by a heterogeneous nucleation of Xe on Ni(111) at 40 K. For Xe growth on Nb(110), due to lattice and symmetry mismatch, Thomas *et al.* observed that a somewhat "disordered" transition layer consisting of two monolayers of Xe was formed first to accommodate the lattice and symmetry mismatch between Nb(110) substrate and a subsequent Xe film that prefers (111) termination.[15] During the subsequent growth of the (111)-terminated Xe film at 40 K, these authors observed a similar but much smaller oscillation in $\Delta_p - \Delta_s$. The line shape of the oscillatory component is characteristic of $\theta_{\mathrm{step}} \propto \sqrt{(1 - Rt)Rt}$ except for a negative sign. The latter can be attributed to $\varepsilon_{d,\mathrm{step}}^{(Xe)} < \varepsilon_{d,\mathrm{terr}}^{(Xe)}$ in Eq. (16). The oscillation comes from a layer-by-layer growth of Xe that was presumably dominated by a homogeneous nucleation.

D. Oxidation of oxide monolayers on SrTiO₃(100) formed by pulsed laser deposition

Zhu and co-workers have done a series of studies on perovskite oxide growth on SrTiO₃(100) using the method of pulsed laser deposition (PLD) in vacuum.[16,20,31,32] They used a combination of reflection high-energy electron-diffraction (RHEED) and OI-RD techniques for *in situ* monitor. Unlike conventional vapor-phase deposition, PLD utilizes laser ablation of a stoichiometric target in front of a substrate for source of deposits. At sufficiently high substrate temperatures and suitable laser-ablation conditions, PLD yields films of high-quality crystalline oxides, judging from sustained oscillations of *in situ* RHEED or surface x-ray diffraction intensity and *ex situ* transmission electron micrograph measurements.[2,5] However, PLD-grown perovskite oxide

films are oxygen deficient and need to be annealed in oxidant ambient after the growth in order to restore the oxygen stoichiometry. The oxidation reaction is kinetically limited and continues even after the film has formed a nearly perfect crystalline structure.

For perovskite oxides, the oxygen deficiency induces extra absorption in the visible range of electromagnetic waves. The extra absorption is reflected in the imaginary part of the optical dielectric constant for visible light.[32] This makes the OI-RD technique a convenient probe to the oxidation state or the chemical makeup of a deposited perovskite oxide monolayer on a stoichiometric substrate.[20,32] When the deposition of a perovskite oxide is interrupted at the completion of one monolayer, the newly crystallized monolayer has an optical dielectric constant $\varepsilon_{d,\mathrm{terr}}$ that may be different from that of the stoichiometric bulk-phase layer $\varepsilon_{d,\mathrm{bulk}}$ due to oxygen deficiency. The OI-RD signal in response to the new monolayer is given by the second term in Eq. (12),

$$\Delta_p - \Delta_s = \alpha_{\mathrm{eff}}(d_{\mathrm{init}}) \frac{[\varepsilon_{d,\mathrm{terr}}(t) - \varepsilon_0][\varepsilon_{d,\mathrm{terr}}(t) - \varepsilon_{s,\mathrm{eff}}(d_{\mathrm{init}})]d_0}{\varepsilon_{d,\mathrm{terr}}(t)}.$$

(19)

During the postgrowth annealing treatment, the oxygen vacancies in the monolayer decrease in number by either reaction with ambient oxidant or transport into the bulk. As a result, $\varepsilon_{d,\mathrm{terr}}(t) = \varepsilon_{d,\mathrm{bulk}} + \delta\varepsilon_{d,\mathrm{terr}}(t)$ continues to evolve until it reaches $\varepsilon_{d,\mathrm{bulk}}$. Particularly, the extra term in the imaginary part of $\varepsilon_{d,\mathrm{terr}}(t)$, $\delta\varepsilon''_{d,\mathrm{terr}}(t)$, is proportional to the surface number density of oxygen vacancies in the monolayer. $\delta\varepsilon''_{d,\mathrm{terr}}(t)$ characterizes the oxidation kinetics and can be directly measured.

For example, Zhu *et al.* studied the homoepitaxy of SrTiO$_3$ monolayers on SrTiO$_3$(100).[32] A stoichiometric SrTiO$_3$(100) is a transparent, insulating substrate with a direct energy gap of 3.2 eV that separates the top of the filled valence band and the bottom of the unoccupied conduction band. The optical dielectric constant of stoichiometric SrTiO$_3$(100) at 633 nm is a real number, $\varepsilon_s = 5.66$. By annealing a stoichiometric SrTiO$_3$ crystal in ultrahigh vacuum, some of oxygen atoms are driven out of the sample, leaving behind oxygen vacancies in the crystal. The photoemission studies reveal that oxygen vacancies in an oxygen-deprived SrTiO$_3$ lead to "impurity" states inside the 3.2-eV band gap, about 1.9 eV below the conduction band. These states are occupied and thus add a small imaginary part to the otherwise real-only optical dielectric constant for an oxygen deficient SrTiO$_3$ crystal. This makes an oxygen-deficient SrTiO$_3$ absorptive in the visible range. For the same reason, a crystallized and yet oxygen-deficient SrTiO$_3$ monolayer on a stoichiometric SrTiO$_3$(100) has an optical dielectric constant $\varepsilon_{d,\mathrm{terr}}(t) = \varepsilon_{d,\mathrm{bulk}} + \delta\varepsilon_{d,\mathrm{terr}}(t)$. The imaginary part $\varepsilon''_{d,\mathrm{terr}}(t) = \delta\varepsilon''_{d,\mathrm{terr}}(t)$ vanishes when the oxygen vacancies are removed during postgrowth annealing in oxygen ambient or by transport into the bulk. In the limit that $\varepsilon''_{d,\mathrm{terr}}(t) \ll \varepsilon'_{d,\mathrm{terr}} \sim \varepsilon_{d,\mathrm{bulk}}$, $\varepsilon''_{d,\mathrm{terr}}(t)$ is easily monitored with Re$\{\Delta_p - \Delta_s\}$,

$$\mathrm{Re}\{\Delta_p - \Delta_s\} \cong \left[|\alpha| d_0 \frac{[\varepsilon'_{d,\mathrm{terr}}(t)]^2 - \varepsilon_s}{[\varepsilon'_{d,\mathrm{terr}}(t)]^2} \right] \varepsilon''_{d,\mathrm{terr}}(t)$$

$$\cong \left[\frac{|\alpha| d_0 (\varepsilon_s - 1)}{\varepsilon_s} \right] \varepsilon''_{d,\mathrm{terr}}(t).$$

(20)

$\varepsilon''_{d,\mathrm{terr}}(t)$ is proportional to the number density of oxygen vacancies in a newly deposited oxide monolayer. By measuring the temporal evolution of Re$\{\Delta_p - \Delta_s\}$, Zhu and co-workers were able to determine the kinetics of oxidation reaction between the ambient oxygen molecules and PLD-deposited SrTiO$_3$ monolayers on SrTiO$_3$(100). Specifically, they found that the oxidation reaction occurs between a surface-bound oxygen vacancy and a chemisorbed O_2^- (the precursor state) near the vacancy. The reaction kinetics is the result of a competition between desorption of O_2^- from the precursor state back to the gas phase and the reaction of O_2^- with the oxygen vacancy. This mechanism was independently proposed by Tanaka *et al.* based on a scanning electron microscopy study of a SrTiO$_3$(100) surface in molecular oxygen ambient.[33]

Chen *et al.* subsequently studied the growth and oxidation of Nb-doped SrTiO$_3$ films on SrTiO$_3$(100).[20] A Nb-doped, stoichiometric SrTiO$_3$ intrinsically absorbs visible light as a result of doping, and thus its bulk-phase optical dielectric constant $\varepsilon_{d,\mathrm{bulk}}$ has an imaginary part at 633 nm. This means that even when oxygen vacancies are removed from an as-grown Nb:SrTiO$_3$ monolayer, $\varepsilon''_{d,\mathrm{terr}}(t)$ approaches a finite value for a stoichiometric Nb:SrTiO$_3$. By measuring $\varepsilon''_{d,\mathrm{terr}}(t) - \varepsilon''_{d,\mathrm{bulk}}(t)$, Chen and co-workers were able to study the kinetics of oxidation of PLD-deposited Nb:SrTiO$_3$ monolayers under low oxygen pressures and in oxygen-free ambient. These authors discovered that even at typical growth temperatures, the transport of oxygen vacancies into the bulk is an alternative way for as-grown Nb:SrTiO$_3$ monolayers to become oxidized. Furthermore, the in-diffusion of oxygen vacancies preferentially takes place at step edges instead of directly into the bulk from terraces.

E. Sustained oscillation in OI-RD signals in response to a continuous layer-by-layer growth of Nb:SrTiO$_3$ on SrTiO$_3$(100) up to hundreds of monolayers

Fei *et al.* demonstrated for the first time that the OI-RD signals have sufficient sensitivity to the variation in surface roughness to reveal a continuous layer-by-layer growth of materials as complex as perovskite oxides.[16] In a steady flow of oxygen ambient, these authors grew over 400 monolayers of Nb:SrTiO$_3$ on SrTiO$_3$(100) in a continuous pulsed laser deposition. The growth was monitored *in situ* with the measurement of Re$\{\Delta_p - \Delta_s\}$. They observed that Re$\{\Delta_p - \Delta_s\}$ exhibited two types of oscillations: one with a large amplitude and a large spatial period equal to half of the optical wavelength (632.8 nm), the other with a small amplitude and a small spatial period equal to the thickness of one monolayer of Nb:SrTiO$_3$ (0.39 nm). The former is a trivial result of thin film optics when the film thickness is comparable to the optical wavelength. The latter is a more subtle optical response to a layer-by-layer growth, or specifically, to an oscillatory

change in step density characteristic of such a growth mode. In this case, $\varepsilon_{d,\text{terr}}$ roughly equals $\varepsilon_{d,\text{bulk}}$ since deposited materials were not given time to become fully oxidized, and the OI-RD signal in response to d_{rough} on top of an initial thickness d_{init} is given by

$$
\Delta_p - \Delta_s = \alpha_{\text{eff}}(d_{\text{init}})
$$
$$
\times \left[\frac{(\varepsilon_{d,\text{bulk}} - \varepsilon_0)[\varepsilon_{d,\text{bulk}} - \varepsilon_{s,\text{eff}}(d_{\text{init}})]d_{\text{rough}}}{\varepsilon_{d,\text{bulk}}} \right.
$$
$$
\left. + \frac{[\varepsilon_{d,\text{step}}\varepsilon_{d,\text{bulk}} - \varepsilon_{s,\text{eff}}(d_{\text{init}})](\varepsilon_{d,\text{step}} - \varepsilon_{d,\text{bulk}})d_0}{\varepsilon_{d,\text{step}}\varepsilon_{d,\text{bulk}}} \theta_{\text{step}} \right].
$$

$$(21)$$

The first term yields a "local envelope" of the OI-RD signal. $\varepsilon_{d,\text{bulk}} - \varepsilon_{s,\text{eff}}(d_{\text{init}})$ decides whether $\Delta_p - \Delta_s$ increases or decreases with d_{rough} (see Appendix A). The second term is oscillatory due to the "periodic" change in θ_{step} typical of a layer-by-layer growth. In the experiment reported by Fei *et al.*, kinetics of growth and oxidation are mixed and were not easily separated. As we will show next, the growth kinetics can be separated from that of oxidation and in turn compared with predictions of growth models. To do so, we find it convenient to interrupt the deposition at the completion of a full monolayer so that the oxidation kinetics can be determined during postdeposition annealing. By proper extrapolation, the contribution from the oxidation kinetics to $\text{Re}\{\Delta_p - \Delta_s\}$ measured *during* growth may be subtracted out, leaving only the step edge dependent term in Eq. (21) for further analysis.

1. Kinetics of perovskite oxide growth studied by in situ OI-RD measurement: Interrupted depositions of Nb:SrTiO₃ monolayers on SrTiO₃(100)

We have studied interrupted deposition and postdeposition annealing of PLD-deposited Nb:SrTiO₃ monolayers on SrTiO₃(100). We use a combination of RHEED and OI-RD techniques as *in situ* probes. Our strategy is to use the full recovery of RHEED intensity as a mark for complete crystallization of a newly deposited monolayer. The subsequent change in $\text{Re}\{\Delta_p - \Delta_s\}$ should come solely from the oxidation process. We determine the kinetics of oxidation during subsequent annealing, and then extrapolate the contribution of oxidation to $\text{Re}\{\Delta_p - \Delta_s\}$ measured during deposition. As a result, we are able to obtain the portion of $\text{Re}\{\Delta_p - \Delta_s\}$ in response to growth kinetics only. The latter can then be compared to predictions of growth models to yield details of growth at a length scale much smaller than the optical wavelength.

In a cycle of interrupted deposition, we grow one monolayer (within ±2%) of 5%-doped Nb:SrTiO₃ and let the as-grown monolayer anneal at the growth temperature of 715 °C in an ambient of molecular oxygen at 1.5×10^{-4} Pa. We monitor the RHEED intensity and the OI-RD signal $\text{Re}\{\Delta_p - \Delta_s\}$ during deposition and subsequent annealing
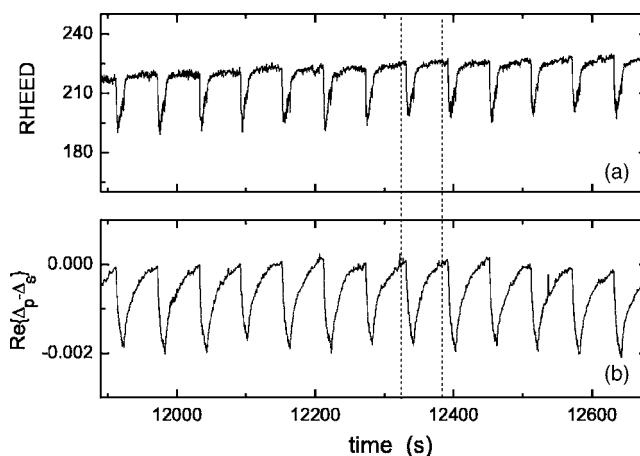
FIG. 7. (a) Reflection high-energy electron-diffraction (RHEED) intensity in response to cycles of interrupted laser deposition of 5%-doped Nb:SrTiO₃ on SrTiO₃(100). The substrate temperature is 715 °C. The ambient molecular oxygen pressure is 1.5×10^{-4} Pa or 1.1×10^{-6} Torr. One ablation laser pulse deposits 0.045 ML of Nb:SrTiO₃ at a rate of 2 Hz so that the mean deposition rate R is 0.105 ML/s, and it takes 9.5 s to deposit one monolayer. The deposition is interrupted immediately after one monolayer and the surface is allowed to anneal for 49 s at 715 °C before the next deposition cycle begins. (b) Simultaneously measured oblique-incidence optical reflectivity difference signal $\text{Re}\{\Delta_p - \Delta_s\}$. The sections between the dotted lines are plotted in Fig. 8.

process. In Fig. 7(a), we display the RHEED intensity in response to a portion of hundreds of interrupted deposition cycles. In Fig. 7(b), we display the corresponding $\text{Re}\{\Delta_p - \Delta_s\}$. The deposition rate is $R = 0.105$ Hz or $\tau = 1/R = 9.5$ s. From RHEED, we learn that at the end of deposition, the surface morphology is not yet fully recovered, indicating that the growth is not a perfect layer-by-layer growth. It takes a few more seconds for RHEED to fully restore to the predeposition level. Afterward, the as-grown Nb:SrTiO₃ monolayer is in essence fully crystallized. However, $\text{Re}\{\Delta_p - \Delta_s\}$ from the growth surface continues to change at a noticeably slower rate.

We zoom in on one interrupted deposition cycle in the middle of Fig. 7(a). In Fig. 8, we display RHEED [Fig. 8(a)] and $\text{Re}\{\Delta_p - \Delta_s\}$ [Fig. 8(b)] for one interrupted deposition cycle with $R = 0.105$ Hz. In this case, the imaginary part of $\varepsilon_{s,\text{eff}}(d_{\text{init}})$ roughly equals to $\varepsilon_{d,\text{bulk}}$ so that $\text{Re}\{\Delta_p - \Delta_s\}$ recovers to the predeposition level after postdeposition annealing (see Appendix A). During deposition, $1 - \theta_0 \approx Rt$ increases until it reaches unity (a full monolayer). The time-dependent portion of $\varepsilon''_{d,\text{terr}}$ is proportional to the density of oxygen vacancies in the newly formed monolayer and diminishes in the course of oxidation that occurs *during* as well as *after* deposition. After the surface morphology is essentially restored so that $\theta_{\text{step}}(t) \sim 0$, the residual $\text{Re}\{\Delta_p - \Delta_s\}$ corresponds to the residual oxygen vacancies and continues to change afterward. We first consider the OI-RD signal during postgrowth annealing,
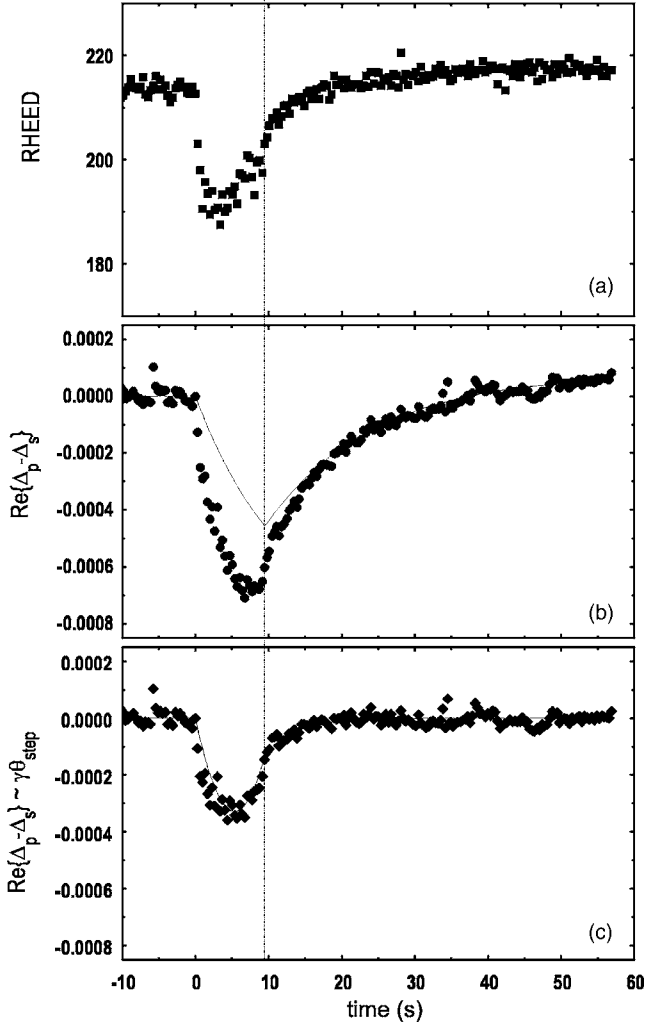
FIG. 8. (a) RHEED intensity in response to one of the interrupted laser deposition cycles as shown in Fig. 7(a). (b) Re$\{\Delta_p - \Delta_s\}$ monitored during the same cycle. The solid line is the contribution from the oxidation of the as-deposited Nb:SrTiO$_3$ layer, obtained by fitting the optical signal during the postcrystallization annealing (see the main text.) (c) Re$\{\Delta_p - \Delta_s\}$ after the contribution from the oxidation [solid line in (b)] is subtracted. The solid line is the calculated Re$\{\Delta_p - \Delta_s\} \cong (2\gamma\sqrt{N_n/N_s})\sqrt{\Delta^2}$ by least-squares fitting (c) to an eight-level growth model described by Eq. (26), together with Eqs. (17) and (18). The fitting parameters are $\eta = 6.1 \pm 0.1$ and $\beta = 0.87 \pm 0.02$. The proportionality constant $(2\gamma\sqrt{N_n/N_s})$ is adjusted to match the optical data.

$$\Delta_p - \Delta_s \cong \alpha_{\text{eff}}(d_{\text{init}})d_0 \frac{[\varepsilon_{d,\text{terr}}(t) - 1][\varepsilon_{d,\text{terr}}(t) - \varepsilon_{s,\text{eff}}(d_{\text{init}})]}{\varepsilon_{d,\text{terr}}(t)}. \tag{22}$$

Since $\varepsilon''_{d,\text{terr}}(t)$ (due to residual oxygen vacancies in the monolayer) and $\varepsilon''_{s,\text{eff}}(d_{\text{init}})$ are both small compared to $\varepsilon'_{d,\text{terr}}(t)$ and $\varepsilon'_{s,\text{eff}}(d_{\text{init}})$, $\alpha_{\text{eff}}(d_{\text{init}})$ is predominantly imaginary. Re$\{\Delta_p - \Delta_s\}$ from Eq. (22) can be simplified as

$$\text{Re}\{\Delta_p - \Delta_s\} \cong |\alpha_{\text{eff}}(d_{\text{init}})|d_0 \left[\left(1 - \frac{\varepsilon'_{s,\text{eff}}(d_{\text{init}})}{\varepsilon'^2_{d,\text{terr}}(t)} \right) \varepsilon''_{d,\text{terr}}(t) \right.$$
$$\left. - \left(1 - \frac{1}{\varepsilon'_{d,\text{terr}}(t)} \right) \varepsilon''_{s,\text{eff}}(d_{\text{init}}) \right] \equiv g(t). \tag{23}$$

The functional form of $g(t)$ is determined from the experiment. From this functional form, we can determine the contribution of oxidation kinetics to the optical signal during the deposition using the following procedure. During the deposition *and* subsequent annealing, we have from Eq. (12) (without the first term)

$$\text{Re}\{\Delta_p - \Delta_s\} \cong \int_0^t H(1/R - t')g(t - t')R dt' + \gamma(t)\theta_{\text{step}}(t). \tag{24}$$

$H(u)$ is the Heaviside unit step function: $H(u > 0) = 1$, while $H(u \leq 0) = 0$. Since the effect of oxygen vacancies in an oxide monolayer is but small compared to the overall optical dielectric response, $\gamma(t) \sim \gamma$ is roughly a constant. From our previous studies on PLD-deposited perovskite monolayers, we find that $g(t) \cong h \exp(-t/\tau_{\text{oxid}})$ is a good approximation. Here, h is proportional to the surface number density of oxygen vacancies in the oxide monolayer. During deposition (i.e., $t < 1/R$) and afterward (i.e., $t > 1/R$), we have

$$\int_0^t H(1/R - t')g(t - t')R dt'$$
$$= \begin{cases} hR\tau_{\text{oxid}}[1 - \exp(-t/\tau_{\text{oxid}})], & t < 1/R \\ hR\tau_{\text{oxid}}[\exp(1/R\tau_{\text{oxid}}) - 1]\exp(-t/\tau_{\text{oxid}}), & t > 1/R. \end{cases} \tag{25}$$

If $g(t)$ as determined experimentally from Eq. (23) is more complicated than an exponential function, one can integrate the right-hand side of Eq. (25) numerically. By fitting the OI-RD signal after the RHEED intensity is fully recovered (with $t > 1/R$), we extract h and τ_{oxid} or the functional form of $g(t)$. Substituting the results into the second part of Eq. (25) for $t < 1/R$, we find the first term in Eq. (24), and in turn the term that is proportional to $\gamma\theta_{\text{step}}(t)$.

We apply this procedure to the experimental data shown in Fig. 8(b). When $t > 20$ s (10 s after the deposition is interrupted), the RHEED is fully recovered, yet Re$\{\Delta_p - \Delta_s\}$ continues to recover. We fit the optical data for $t > 20$ s to the second part of Eq. (25) and extrapolate the fit to the remaining part of Eq. (25) ($0 < t < 20$ s) using the procedure outlined above. The result is shown in solid line in Fig. 8(b). Subtracting the fit from Re$\{\Delta_p - \Delta_s\}$, we obtain the remainder of Re$\{\Delta_p - \Delta_s\}$ as now displayed in Fig. 8(c). From Eq. (24), this part of Re$\{\Delta_p - \Delta_s\}$ is proportional to the surface density of unit cells at step edges.

From Eqs. (17) and (18), it is clear that up to a constant the OI-RD signal as displayed in Fig. 8(c) is a direct measure of surface roughness, a key characteristic of surface morphology. Surface roughness is a result of the balance of growth kinetics and growth conditions such as deposition, intralayer mass transport, interlayer mass transport, heteroge-

neity of the surface, and surfactants. For different growth models, surface roughness varies with the amount of the deposited materials differently. As a result, the OI-RD signal as shown in Fig. 8(c) yields detailed information on the growth.

We should note that except for thermal helium atoms, specular reflection of electrons or x-ray photons even under weak antiphase conditions measures the reduction of specular reflection due to destructive interference of reflected wavelets from adjacent terraces instead of surface roughness.[1–5] The OI-RD measurement at least complements electron or surface x-ray diffraction measurements. The OI-RD data enable a convenient analysis of surface morphology as a result of growth kinetics because the roughness given by Eq. (18) is a simple outcome of a growth model. In the next section, we will apply an eight-level growth model to the epitaxy of $Nb:SrTiO_3$ on $SrTiO_3(100)$ by fitting the data in Fig. 8(c).

2. Multilevel birth-death model of growth for $Nb:SrTiO_3$ epitaxy on $SrTiO_3(100)$

We use an eight-level growth model similar to the one used by van der Vegt *et al.* to analyze the growth of $Nb:SrTiO_3$.[34] There are four major processes that determine the distribution of terraces at different levels: deposition (with a rate R), intralayer transport, interlayer transport, and the Ostwald ripening.[35] The Ostwald ripening, not negligible during the growth of $Nb:SrTiO_3$ on $SrTiO_3(100)$ in our study, was not considered in the model used by van der Vegt *et al.* In our formulation of the eight-level model, we include the effect of Ostwald ripening in a simplified way that is commensurate with how the mass transport is treated.

In this model, we assume that a fixed fraction β of newly deposited unit cells on a terrace (level) makes it to the lower adjacent terrace (level). The remaining fraction $1-\beta$ of the deposited unit cells stay on the terrace of arrival. The Ostwald ripening makes an upper terrace disintegrate until its lower adjacent terrace is filled up. The disintegration is driven by the Gibbs-Thompson effect.[35] We should note that our definition of the jth level coverage $\theta_j = \theta_{j,t} + \theta_{j,step}$ is the "exposed" part of the level instead of its "footprint" Θ_j of the level as conventionally adopted in the literature. We will compute Θ_j first, and then find $\theta_j \equiv \Theta_j - \Theta_{j+1}$. We write down the rate equations for Θ_j up to eight terraces (levels) as follows:[34,35]

$$d\Theta_1/dt = R(1-\Theta_1) + \beta[R(\Theta_1-\Theta_2) + \eta\Theta_2]H(1-\Theta_1),$$
(26a)

$$d\Theta_j/dt = R(\Theta_{j-1}-\Theta_j) + \beta[R(\Theta_j-\Theta_{j+1}) + \eta\Theta_{j+1}]H(1-\Theta_j)$$
$$- \beta[R(\Theta_{j-1}-\Theta_j) + \eta\Theta_j]H(1-\Theta_{j-1}) \quad (1 < j < 8),$$
(26b)

$$d\Theta_8/dt = R(\Theta_7-\Theta_8) + R\Theta_8 - \beta[R(\Theta_7-\Theta_8) + \eta\Theta_8]$$
$$\times H(1-\Theta_7).$$
(26c)
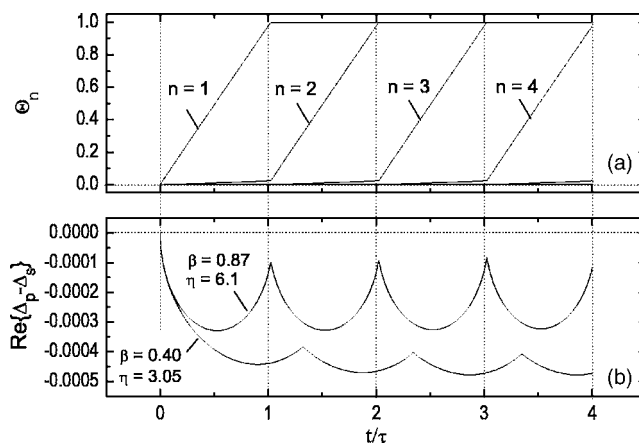
FIG. 9. (a) Coverage or footprint of various levels (terraces) Θ_j for $j=1-8$ vs normalized deposition time or deposited materials in unit of monolayers during a continuous growth. Θ_j's are calculated using the eight-level model (see the main text) with the parameters $\eta=6.1\pm0.1$ and $\beta=0.87\pm0.02$, obtained from fitting Fig. 8(c). (b) Corresponding $Re\{\Delta_p-\Delta_s\} \cong (2\gamma\sqrt{N_n/N_s})\sqrt{\Delta^2}$ during the continuous growth using $\theta_j = \Theta_j - \Theta_{j+1}$ and Eqs. (17) and (18) with $\eta=6.1$ and $\beta=0.87$. The proportionality constant $(2\gamma\sqrt{N_n/N_s})$ is the same as used in the calculation of the solid line in Fig. 8(c). Also shown is the calculated $Re\{\Delta_p-\Delta_s\} \cong (2\gamma\sqrt{N_n/N_s})\sqrt{\Delta^2}$ with $\eta=3.1$ and $\beta=0.4$, suitable for a continuous growth at a lower temperature as in Ref. 16.

The η-dependent terms come from disintegration of upper terraces driven by Gibbs-Thompson effect or Ostwald ripening as long as lower terraces are not filled[36,37] When β is unity so that all the atoms deposited on an upper terrace make it to the lower terrace until the latter fully covers the surface, we have a perfect layer-by-layer growth. When β is less than unity, we have a quasi-layer-by-layer growth as in most cases. Equation (26) are solved with the initial conditions $\Theta_1(0)=0$, $\Theta_2(0)=0$, $\Theta_3(0)=0$, $\Theta_4(0)=0$, $\Theta_5(0)=0$, $\Theta_6(0)=0$, $\Theta_7(0)=0$, $\Theta_8(0)=0$, and $R=0.1$ Hz. β and η are adjusted to least-square fit the solution of Eq. (26) to the OI-RD signal in Fig. 8(c). The fit yields $\eta=6.1\pm0.1$ and $\beta=0.87\pm0.02$. The closeness of β to unity is a measure of the closeness of the growth to a perfect layer-by-layer mode. These two parameters can be used to compute the OI-RD signal in a continuous growth.[16] In Fig. 9(a), we show Θ_n ($n=1-8$) vs normalized time $t/\tau = Rt$ in a continuous deposition computed from the eight-level model with $\eta=6.1\pm0.1$ and $\beta=0.87\pm0.02$. The corresponding OI-RD signals $Re\{\Delta_p-\Delta_s\}$ are displayed in Fig. 9(b). The optical signals show oscillatory behaviors, similar to the observation made by Fei *et al.*[16] of a continuous growth of 10%-doped $Nb:SrTiO_3$ on $SrTiO_3(100)$ (shown in Fig. 10). In their study, the substrate temperature was 655 °C, lower than the temperature that yielded the parameters $\eta=6.1$ and $\beta=0.87$. As a result, smaller β and η should be expected in their case. Indeed, the magnitude of the oscillation observed by Fei *et al.* is better represented by the calculation with $\beta=0.4$ and $\eta=3.1$, as displayed in Fig. 9(b).
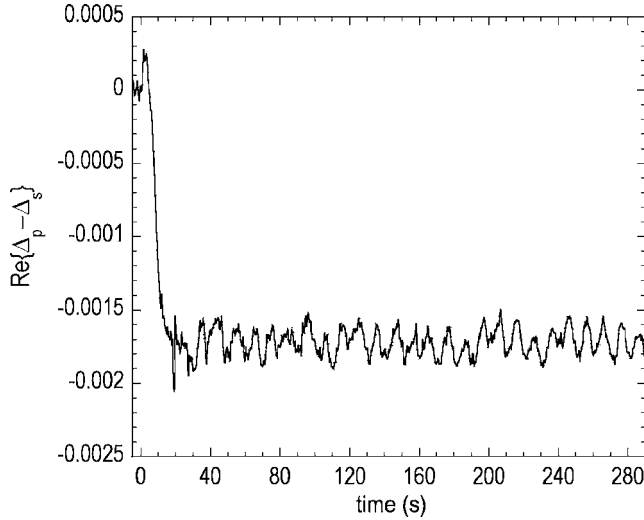
FIG. 10. $\text{Re}\{\Delta_p - \Delta_s\}$ vs time in response to deposition of the first 28 monolayers in a continuous growth of 10 mol. % doped $\text{Nb}:\text{SrTiO}_3$ on $\text{SrTiO}_3(100)$ under a pulsed laser deposition condition, measured by Fei *et al.* (Ref. [16]). The substrate temperature is held at 655 °C. The ambient molecular oxygen pressure is 2 $\times 10^{-6}$ Torr. The deposition rate is roughly $R=0.1$ Hz or 0.1 ML/s. The envelope part of $\text{Re}\{\Delta_p - \Delta_s\}$ [corresponding to the first term in Eq. (21)] has been subtracted out so that only the step edge density dependent term is left for comparison with the prediction of a growth model as displayed in Fig. 9(b).

IV. SUMMARY

We developed a mean-field model to describe the oblique-incidence optical reflectivity difference in response to the presence of an atomically rough and yet optical smooth film on a solid surface. The reflectivity difference $\Delta_p - \Delta_s$ as defined in Eq. (6) is directly measurable, and is related to the standard ellipsometry ratio $r_p/r_s = \tan\psi\exp(i\delta)$ by $\Delta_p - \Delta_s = \Delta\psi/(\cos\psi_0\sin\psi_0) + i\Delta\delta$. We find that $\Delta_p - \Delta_s$ depends on the morphology and chemical makeup of a thin film in a tractable way such that quantitative information on the film can be deduced and followed in real time from carefully designed optical measurements. Because an optical technique is inherently more versatile in terms of implementation and requirement on thin-film deposition conditions, the oblique-incidence reflectivity difference technique (OI-RD) is becoming an analytical technique for *in situ* characterization of various types of thin films on solids.

APPENDIX A: OPTICAL REFLECTIVITY DIFFERENCE FROM A FOUR-LAYER SYSTEM

We consider a four-layer system as shown Fig. 11. It consists of a semi-infinite ambient with ε_0, an optically thin
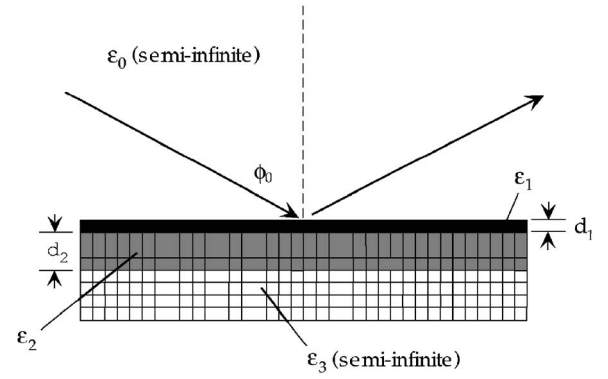
FIG. 11. Sketch of a four-layer system that consists of an ambient with ε_0, a smooth and *optically thin* film with thickness d_1 and optical dielectric constant ε_1 (black squares), a smooth film with thickness d_2 and optical dielectric constant ε_2 (dark gray squares), and a semi-infinite substrate with optical dielectric constant ε_3 (white squares). Dark gray squares: atoms inside the film, characterized by $\varepsilon_{d,\text{bulk}}$. Black squares: terrace atoms, characterized by $\varepsilon_{d,\text{terr}}$. The system is illuminated with a collimated, monochromatic light beam from the ambient with ε_0 at an incidence angle ϕ_0.

layer with ε_1 and d_1, an arbitrarily thick layer with ε_2 and d_2, and a semi-infinite substrate with ε_3.

Let a monochromatic light beam with a vacuum wavelength λ be incident on such a system from the ambient at an angle of ϕ_0. The incidence angles in the remaining three media, ϕ_1, ϕ_2, and ϕ_3, can be determined by Snell's law,

$$\sqrt{\varepsilon_0}\sin\phi_0 = \sqrt{\varepsilon_1}\sin\phi_1 = \sqrt{\varepsilon_2}\sin\phi_2 = \sqrt{\varepsilon_3}\sin\phi_3.$$
(A1)

Let $r_s(\varepsilon_0;\varepsilon_1,d_1;\varepsilon_2,d_2;\varepsilon_3)$ and $r_p(\varepsilon_0;\varepsilon_1,d_1;\varepsilon_2,d_2;\varepsilon_3)$ be the reflectivities for the s-polarized and p-polarized components of the incident beam. We define

$$\Delta_p(\varepsilon_0;\varepsilon_1,d_1;\varepsilon_2,d_2;\varepsilon_3)$$
$$\equiv \frac{r_p(\varepsilon_0;\varepsilon_1,d_1;\varepsilon_2,d_2;\varepsilon_3) - r_p(\varepsilon_0;\varepsilon_1,d_1=0;\varepsilon_2,d_2;\varepsilon_3)}{r_p(\varepsilon_0;\varepsilon_1,d_1=0;\varepsilon_2,d_2;\varepsilon_3)},$$
(A2)

$$\Delta_s(\varepsilon_0;\varepsilon_1,d_1;\varepsilon_2,d_2;\varepsilon_3)$$
$$\equiv \frac{r_s(\varepsilon_0;\varepsilon_1,d_1;\varepsilon_2,d_2;\varepsilon_3) - r_s(\varepsilon_0;\varepsilon_1,d_1=0;\varepsilon_2,d_2;\varepsilon_3)}{r_s(\varepsilon_0;\varepsilon_1,d_1=0;\varepsilon_2,d_2;\varepsilon_3)}.$$
(A3)

Our goal is to compute the optical reflectivity difference defined as

$$\Delta_p(\varepsilon_0;\varepsilon_1,d_1;\varepsilon_2,d_2;\varepsilon_3) - \Delta_s(\varepsilon_0;\varepsilon_1,d_1;\varepsilon_2,d_2;\varepsilon_3)$$ (A4)

in the limit of $d_1 \ll \lambda$.

It is straightforward to derive $r_s(\varepsilon_0;\varepsilon_1,d_1;\varepsilon_2,d_2;\varepsilon_3)$ and $r_p(\varepsilon_0;\varepsilon_1,d_1;\varepsilon_2,d_2;\varepsilon_3)$ using the standard matrix method.[31,32]

Since $d_1 \ll \lambda$, we expand the results and only keep terms up to the first order of d_1/λ. The zeroth-order term in $r_s(\varepsilon_0; \varepsilon_1, d_1; \varepsilon_2, d_2; \varepsilon_3)$ is $r_s(\varepsilon_0; \varepsilon_1, d_1=0; \varepsilon_2, d_2; \varepsilon_3)$, and the zeroth-order term in $r_p(\varepsilon_0; \varepsilon_1, d_1; \varepsilon_2, d_2; \varepsilon_3)$ is $r_p(\varepsilon_0; \varepsilon_1, d_1=0; \varepsilon_2, d_2; \varepsilon_3)$. We can then compute $\Delta_p(\varepsilon_0; \varepsilon_1, d_1; \varepsilon_2, d_2; \varepsilon_3) - \Delta_s(\varepsilon_0; \varepsilon_1, d_1; \varepsilon_2, d_2; \varepsilon_3)$ using Eqs. (A1) and (A2). After some algebraic arrangement of the terms, we find

$$
\Delta_p(\varepsilon_0; \varepsilon_1, d_1; \varepsilon_2, d_2; \varepsilon_3) - \Delta_s(\varepsilon_0; \varepsilon_1, d_1; \varepsilon_2, d_2; \varepsilon_3)
$$
$$
= \alpha(\varepsilon_0; \varepsilon_2, d_2; \varepsilon_3) d_1 \frac{(\varepsilon_1 - \varepsilon_0)[\varepsilon_1 - \varepsilon_3(\varepsilon_0; \varepsilon_2, d_2; \varepsilon_3)]}{\varepsilon_1}.
$$
(A5)

The functions cited in Eq. (A5) are given by

$$
\alpha(\varepsilon_0; \varepsilon_2, d_2; \varepsilon_3) = (-i)\frac{4\pi\sqrt{\varepsilon_0}\cos\phi_0}{\lambda} \frac{\varepsilon_0 A_{23} C_{23} \sin^2\phi_0 \cos^2\phi_2 + \varepsilon_2(B_{23}C_{23}\cos^2\phi_0 - A_{23}D_{23}\cos^4\phi_2)}{(\varepsilon_0^2 A_{23}C_{23} + \varepsilon_2^2 B_{23}D_{23})\cos^2\phi_0\cos^2\phi_2 + \varepsilon_0\varepsilon_2(A_{23}D_{23}\cos^4\phi_2 + B_{23}C_{23}\cos^4\phi_0)},
$$
(A6)

$$
\varepsilon_3(\varepsilon_0; \varepsilon_2, d_2; \varepsilon_3) = \frac{\varepsilon_2 B_{23}\sin^2\phi_0(\varepsilon_2 D_{23}\cos^2\phi_2 + \varepsilon_0 C_{23}\cos^2\phi_0)}{\varepsilon_0 A_{23} C_{23}\sin^2\phi_0\cos^2\phi_2 + \varepsilon_2(B_{23}C_{23}\cos^2\phi_0 - A_{23}D_{23}\cos^4\phi_2)}.
$$
(A7)

The coefficients in Eqs. (A6) and (A7) are given by the following expressions:

$$
A_{23} = + \left[\sqrt{\varepsilon_2}\cos\phi_3\cos\left(\frac{2\pi\sqrt{\varepsilon_2}d_2\cos\phi_2}{\lambda}\right) \right.
$$
$$
\left. - i\sqrt{\varepsilon_3}\cos\phi_2\sin\left(\frac{2\pi\sqrt{\varepsilon_2}d_2\cos\phi_2}{\lambda}\right) \right]^2,
$$
(A8a)

$$
B_{23} = - \left[\sqrt{\varepsilon_3}\cos\phi_2\cos\left(\frac{2\pi\sqrt{\varepsilon_2}d_2\cos\phi_2}{\lambda}\right) \right.
$$
$$
\left. - i\sqrt{\varepsilon_2}\cos\phi_3\sin\left(\frac{2\pi\sqrt{\varepsilon_2}d_2\cos\phi_2}{\lambda}\right) \right]^2,
$$
(A8b)

$$
C_{23} = + \left[\sqrt{\varepsilon_2}\cos\phi_2\cos\left(\frac{2\pi\sqrt{\varepsilon_2}d_2\cos\phi_2}{\lambda}\right) \right.
$$
$$
\left. - i\sqrt{\varepsilon_3}\cos\phi_3\sin\left(\frac{2\pi\sqrt{\varepsilon_2}d_2\cos\phi_2}{\lambda}\right) \right]^2,
$$
(A8c)

$$
D_{23} = - \left[\sqrt{\varepsilon_3}\cos\phi_3\cos\left(\frac{2\pi\sqrt{\varepsilon_2}d_2\cos\phi_2}{\lambda}\right) \right.
$$
$$
\left. - i\sqrt{\varepsilon_2}\cos\phi_2\sin\left(\frac{2\pi\sqrt{\varepsilon_2}d_2\cos\phi_2}{\lambda}\right) \right]^2.
$$
(A8d)

Equation (A5) has the same form as Eq. (9) in Ref. 23, except that α [defined by Eq. (10) in Ref. 23] is generalized to $\alpha(\varepsilon_0; \varepsilon_2, d_2; \varepsilon_3)$ and ε_s is generalized to $\varepsilon_3(\varepsilon_0; \varepsilon_2, d_2; \varepsilon_3)$. It is easily verified that when $d_2 \to 0$, $\varepsilon_3(\varepsilon_0; \varepsilon_2, d_2; \varepsilon_3) \to \varepsilon_3$, $\alpha(\varepsilon_0; \varepsilon_2, d_2; \varepsilon_3) \to \alpha$, and thus Eq. (A5) returns to Eq. (11) of Ref. 23 with $\varepsilon_s = \varepsilon_3$. It is also readily verified that when $d_2 \to \infty$, $\varepsilon_3(\varepsilon_0; \varepsilon_2, d_2; \varepsilon_3) \to \varepsilon_2$, $\alpha(\varepsilon_0; \varepsilon_2, d_2; \varepsilon_3) \to \alpha$, so that Eq. (A5) again returns to Eq. (11) of Ref. 23 with $\varepsilon_s = \varepsilon_2$.

To evaluate the specific effect of finite bulk-phase film d_2 on the OI-RD signals measured in the heteroepitaxy of $\mathrm{Nb}:\mathrm{SrTiO_3}$ on $\mathrm{SrTiO_3}(100)$, it is useful to numerically calculate $\alpha(\varepsilon_0; \varepsilon_2, d_2; \varepsilon_3)$ and $\varepsilon_3(\varepsilon_0; \varepsilon_2, d_2; \varepsilon_3)$ vs d_2 with the specific choices of $\varepsilon_0 = 1$, $\varepsilon_2 = 5.29 + i0.46$, $\varepsilon_3 = 5.66$, and the experimental incidence angle $\phi_0 \cong 81°$.[16] The *analytical* forms of Eqs. (A6) and (A7) are not very revealing for us to distinguish the contributions from $\alpha(\varepsilon_0; \varepsilon_2, d_2; \varepsilon_3)$ and $\varepsilon_3(\varepsilon_0; \varepsilon_2, d_2; \varepsilon_3)$ to the OI-RD signals when d_2 is finite.

In Fig. 12, we plot the real and imaginary parts of $\alpha(\varepsilon_0; \varepsilon_2, d_2; \varepsilon_3)$ vs d_2 of a bulk-phase $\mathrm{Nb}:\mathrm{SrTiO_3}$ film on $\mathrm{SrTiO_3}(100)$. Because the imaginary part of $\varepsilon_2 = 5.29 + i0.46$ is much smaller than the real part, $\alpha(\varepsilon_0; \varepsilon_2, d_2; \varepsilon_3)$ is predominantly imaginary and more or less a constant. As a result, $\mathrm{Re}\{\Delta_p - \Delta_s\}$ deduced from Eq. (A5) is dominated by the
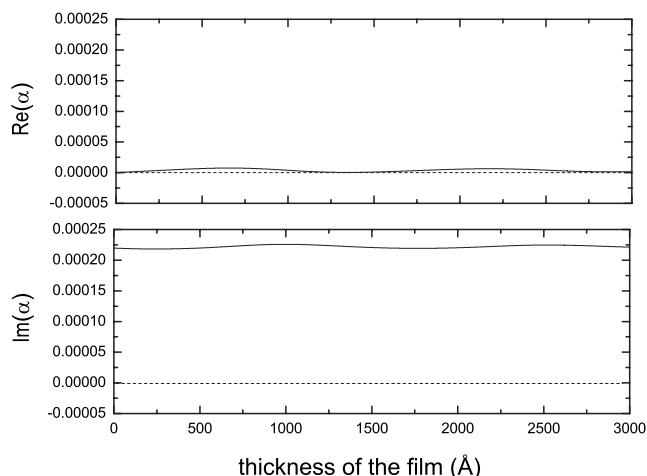
FIG. 12. Real and imaginary parts of $\alpha(\varepsilon_0; \varepsilon_2, d_2; \varepsilon_3)$ vs d_2 computed using $\varepsilon_0 = 1$, $\varepsilon_2 = 5.29 + i0.46$, $\varepsilon_3 = 5.66$, and the experimental incidence angle $\phi_0 \cong 81°$. $\alpha(\varepsilon_0; \varepsilon_2, d_2; \varepsilon_3)$ is defined by Eq. (A6) in Appendix A.
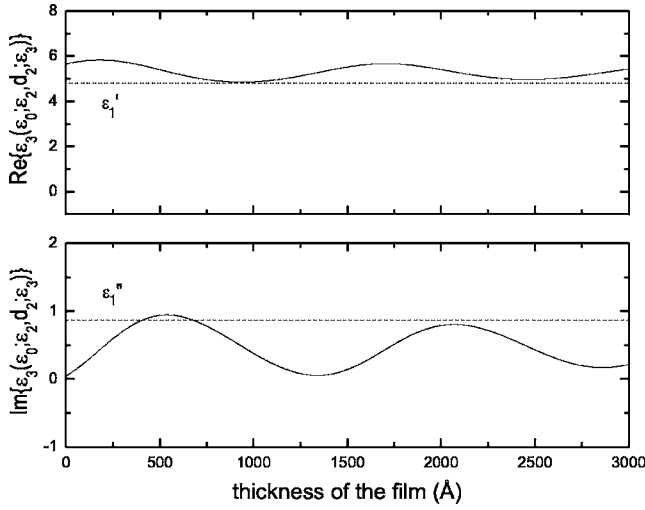
FIG. 13. Real and imaginary parts of $\varepsilon_3(\varepsilon_0;\varepsilon_2,d_2;\varepsilon_3)$ vs d_2 computed using $\varepsilon_0=1$, $\varepsilon_2=5.29+i0.46$, $\varepsilon_3=5.66$, and the experimental incidence angle $\phi_0\cong 81°$. $\varepsilon_3(\varepsilon_0;\varepsilon_2,d_2;\varepsilon_3)$ is defined by Eq. (A7) in Appendix A.

imaginary part of $(\varepsilon_1-\varepsilon_0)[\varepsilon_1-\varepsilon_3(\varepsilon_0;\varepsilon_2,d_2;\varepsilon_3)]/\varepsilon_1$ and can be simplified as

$$\mathrm{Re}\{\Delta_p-\Delta_s\}\cong|\alpha(\varepsilon_0;\varepsilon_2,d_2;\varepsilon_3)|d_0\left[\left(1-\frac{\varepsilon_3'(\varepsilon_0;\varepsilon_2,d_2;\varepsilon_3)}{\varepsilon_1'^2}\right)\varepsilon_1''\right.$$
$$\left.-\left(1-\frac{1}{\varepsilon_1'}\right)\varepsilon_3''(\varepsilon_0;\varepsilon_2,d_2;\varepsilon_3)\right].\quad (A9)$$

We can see that the difference $\varepsilon_1''-\varepsilon_3''(\varepsilon_0;\varepsilon_2,d_2;\varepsilon_3)$ essentially determines whether $\mathrm{Re}\{\Delta_p-\Delta_s\}$ increases or decreases with the addition of a new monolayer Nb:SrTiO$_3$ film (characterized by ε_1) on top of a bulk-phase Nb:SrTiO$_3$ film. This is illustrated in Figs. 13 and 14. In Fig. 13, we plot $\varepsilon_3(\varepsilon_0;\varepsilon_2,d_2;\varepsilon_3)$ vs the thickness d_2 of a bulk-phase Nb:SrTiO$_3$ film with $\varepsilon_2=5.29+i0.46$ on SrTiO$_3$(100) with $\varepsilon_3=5.66$. When a monolayer film with $\varepsilon_1=4.84+i0.88$ and $d_1=3.9$ Å is deposited on top of the bulk-phase Nb:SrTiO$_3$ film, the corresponding $\Delta_p-\Delta_s$ is shown in Fig. 14. The dash lines in Fig. 13 mark the real and imaginary parts of $\varepsilon_1=4.84+i0.88$. Clearly, the sign of $\mathrm{Re}\{\Delta_p-\Delta_s\}$ is determined by whether ε_1'' is larger or smaller than $\varepsilon_3''(\varepsilon_0;\varepsilon_2,d_2;\varepsilon_3)$, and the magnitude of $\mathrm{Re}\{\Delta_p-\Delta_s\}$ is proportional to that of $\varepsilon_1''-\varepsilon_3''(\varepsilon_0;\varepsilon_2,d_2;\varepsilon_3)$. In fact, the sign of $\mathrm{Im}\{\Delta_p-\Delta_s\}$ is also determined by whether ε_1' is larger or smaller than $\varepsilon_1'(\varepsilon_0;\varepsilon_2,d_2;\varepsilon_3)$, and the magnitude of $\mathrm{Im}\{\Delta_p-\Delta_s\}$ is basically determined by the magnitude of $\varepsilon_1'-\varepsilon_3'(\varepsilon_0;\varepsilon_2,d_2;\varepsilon_3)$.

APPENDIX B: DENSITY OF STEP EDGES VS ROUGHNESS OF A GROWTH SURFACE

The density of step edges is related to the roughness of a crystalline solid surface through the mean slope of the surface $\langle|m|\rangle$ to be defined below. For simplicity, we consider a surface of a simple cubic solid with a lattice constant a_0, as shown in Fig. 15. On average, the surface coincides with the x-y plane of the coordinate system. Let $h(x_i,y_j)$ be the height
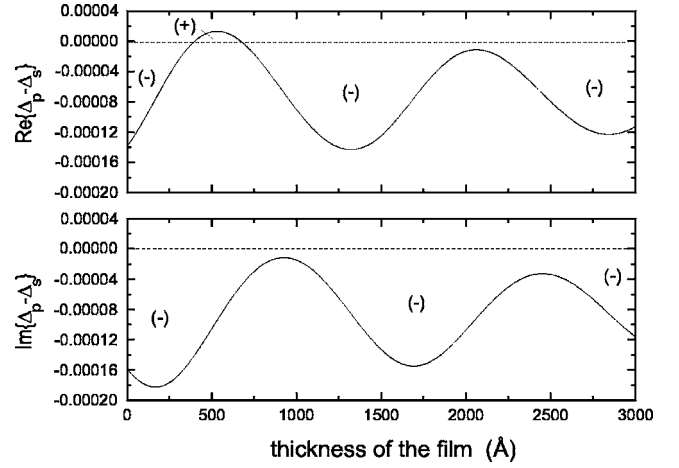
FIG. 14. Changes in real and imaginary parts of $\Delta_p-\Delta_s$ $=\alpha(\varepsilon_0;\varepsilon_2,d_2;\varepsilon_3)d_1(\varepsilon_1-\varepsilon_0)[\varepsilon_1-\varepsilon_3(\varepsilon_0;\varepsilon_2,d_2;\varepsilon_3)]/\varepsilon_1$ vs the thickness d_2 of a bulk-phase Nb:SrTiO$_3$ film with $\varepsilon_2=5.29+i0.46$ when a monolayer Nb:SrTiO$_3$ film with $\varepsilon_1=4.84+i0.88$ and $d_1=3.9$ Å is deposited on top of the bulk-phase film. $\alpha(\varepsilon_0;\varepsilon_2,d_2;\varepsilon_3)$ is given in Fig. 12 and $\varepsilon_3(\varepsilon_0;\varepsilon_2,d_2;\varepsilon_3)$ in Fig. 13. The OI-RD signal increases for $(+)$ sign and decreases for $(-)$ sign with the addition of the new monolayer.

of a surface atom or the center of a surface unit cell with coordinates x_i and y_j. The local slope can be defined as

$$\vec{m}(x_i,y_j)=\frac{h(x_i,y_j)-h(x_{i-1},y_j)}{a_0}\hat{x}+\frac{h(x_i,y_j)-h(x_i,y_{j-1})}{a_0}\hat{y}\quad (B1)$$

and it is a vector. The average of the local slope over a macroscopic area is zero by the choice of the coordinate frame. We can define the mean slope as the average of the magnitude of the local slope,

$$\langle|m|\rangle=\frac{1}{2N_s}\sum_{i=1}^{\sqrt{N_s}}\sum_{j=1}^{\sqrt{N_s}}\left[\frac{|h(x_i,y_j)-h(x_{i-1},y_j)|}{a_0}\right.$$
$$\left.+\frac{|h(x_i,y_j)-h(x_i,y_{j-1})|}{a_0}\right].\quad (B2)$$

We note that $|h(x_i,y_j)-h(x_{i-1},y_j)|/a_0$ or $|h(x_i,y_j)$
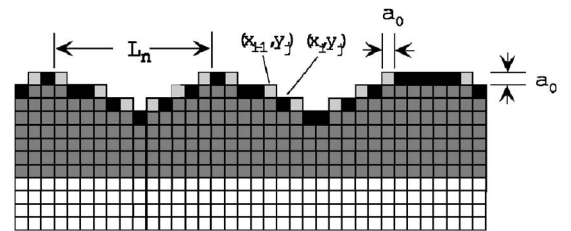
FIG. 15. Sketch of a crystalline film on a substrate (white squares) with a simple square lattice. The lattice constant is a_0. Dark gray squares are unit cells inside the film. Black squares are terrace-bound unit cells. Light gray squares are step-edge-bound unit cells. The mean separation between two neighboring islands is L_n that is related to the saturation nucleation density N_n by $L_n=1/\sqrt{N_n}$. The mean slope $\langle|m|\rangle$ of the surface is roughly the ratio of the rms roughness to one-half of L_n.

$-h(x_i, y_{j-1})|/a_0$ equals unity when the summation goes through a step edge while vanishes elsewhere. As a result, the summation equals twice the number of atoms or unit cells at step edges per unit area, $2N_s^{(\text{step})}$, and we have

$$\langle|m|\rangle = \frac{N_s^{(\text{step})}}{N_s} \equiv \theta_{\text{step}}. \qquad (B3)$$

The mean slope is related to the roughness of the surface as defined by Eq. (18) in the main text. The formation of a monolayer crystalline film on a solid surface proceeds in three phases: nucleation, growth, and coalescence. During nucleation, stable nuclei grow in number until their number reaches a saturation density N_n. At this point, the coverage of the film is still far below one monolayer. Subsequently, the stable nuclei grow in size but only until the coalescence sets in. This means that the average separation between neighboring stable nuclei is $L_n = 1/\sqrt{N_n}$, and the mean slope of such a surface is given by

$$\langle|m|\rangle \cong \frac{\sqrt{\Delta^2}a_0}{(L_n/2)} = 2\sqrt{N_n/N_s}\sqrt{\Delta^2}. \qquad (B4)$$

Combining Eqs. (B3) and (B4), we arrive at

$$\theta_{\text{step}} \cong 2\sqrt{N_n/N_s}\sqrt{\Delta^2}. \qquad (B5)$$

*FAX: +1-530/752-4717. Electronic address: xdzhu@physics.ucdavis.edu

[1] J. H. Neave, B. A. Joyce, P. J. Dobson, and N. Norton, Appl. Phys. A: Solids Surf. **31**, 1 (1983); P. J. Dobson, N. G. Norton, J. H. Neave, and B. A. Joyce, Vacuum **33**, 593 (1983); T. Sakamoto, N. J. Kawai, T. Nakagawa, K. Ohta, T. Kojima, and G. Hashiguchi, Surf. Sci. **174**, 651 (1986); J. M. Van Hove, P. R. Pukite, and P. I. Cohen, J. Vac. Sci. Technol. B **3**, 563 (1985).

[2] M. Kawasaki, K. Takahashi, T. Maeda, R. Tsuchiya, M. Shinohara, O. Ishiyama, T. Yonezawa, M. Yoshimoto, and H. Koinuma, Science **266**, 1540 (1994); G. J. H. M. Rijnders, G. Koster, D. H. A. Blank, and H. Rogalla, Appl. Phys. Lett. **70**, 1888 (1997).

[3] J. H. Haeni, C. D. Theis, and D. G. Schlom, J. Electroceram. **4**, 385 (2000).

[4] B. Poelsema and G. Comsa, *Scattering of Thermal Energy Atoms* (Springer-Verlag, Berlin, 1989).

[5] E. Vlieg, A. W. Denier van der Gon, J. F. van der Veen, J. E. Macdonald, and C. Norris, Phys. Rev. Lett. **61**, 2241 (1988); G. Eres, J. Z. Tischler, M. Yoon, B. C. Larson, C. M. Rouleau, D. H. Lowndes, and P. Zschack, Appl. Phys. Lett. **80**, 3379 (2002).

[6] J. A. Stroscio, D. T. Pierce, and R. A. Dragoset, Phys. Rev. Lett. **70**, 3615 (1993).

[7] G. Rosenfeld, B. Poelsema, and G. Comsa, in *Growth and Properties of Ultrathin Epitaxial Layers*, edited by D. A. King and D. P. Woodruff (Elsevier Science B. V., Amsterdam, 1997), p. 66.

[8] N. Kobayashi and Y. Horikoshi, Jpn. J. Appl. Phys., Part 2 **29**, L702 (1990).

[9] D. E. Aspnes, W. E. Quinn, and S. Gregory, J. Vac. Sci. Technol. A **9**, 870 (1991).

[10] J. F. McGilp, Prog. Surf. Sci. **49**, 1 (1995).

[11] I. Kamiya, L. Mantese, D. E. Aspnes, D. W. Kisker, P. H. Fuoss, G. B. Stephenson, and S. Brennan, J. Cryst. Growth **163**, 67 (1996).

[12] D. E. Aspnes and N. Dietz, Appl. Surf. Sci. **130–132**, 367 (1998).

[13] M. Ebert, K. A. Bell, K. Flock, and D. E. Aspnes, Phys. Status Solidi A **184**, 79 (2001).

[14] L. Bleckmann, O. Hunderi, W. Richter, and E. Wold, Surf. Sci. **351**, 277 (1996).

[15] P. Thomas, E. Nabighian, M. C. Bartelt, C. Y. Fong, and X. D. Zhu, Appl. Phys. A: Mater. Sci. Process. **79**, 131 (2004).

[16] Y. Y. Fei, X. D. Zhu, L. F. Liu, H. B. Lu, Z. H. Chen, and G. Z. Yang, Phys. Rev. B **69**, 233405 (2004).

[17] A. Wong and X. D. Zhu, Appl. Phys. A: Mater. Sci. Process. **63**, 1 (1996).

[18] E. Nabighian, M. C. Bartelt, and X. D. Zhu, Phys. Rev. B **62**, 1619 (2000).

[19] X. D. Zhu and E. Nabighian, Appl. Phys. Lett. **73**, 2736 (1998).

[20] F. Chen, T. Zhao, Y. Y. Fei, H. B. Lu, Z. H. Chen, G. Z. Yang, and X. D. Zhu, Appl. Phys. Lett. **80**, 2889 (2002); X. D. Zhu, Y. Y. Fei, H. B. Lu, and G. Z. Yang, *ibid.* **87**, 051903 (2005).

[21] J. P. Landry, X. D. Zhu, and J. Gregg, Opt. Lett. **29**, 581 (2004).

[22] W. Schwarzacher, J. Gray, and X. D. Zhu, Electrochem. Solid-State Lett. **6**, C73 (2003).

[23] X. D. Zhu, Phys. Rev. B **69**, 115407 (2004).

[24] S. Stoyanov and M. Michailov, Surf. Sci. **202**, 109 (1988).

[25] Y. Y. Fei, P. Thomas, and X. D. Zhu, Appl. Phys. A: Mater. Sci. Process. **86**, 115 (2006).

[26] Y. Y. Fei and X. D. Zhu, Europhys. Lett. **76**, 877 (2006).

[27] G. Y. Wu, S.-E. Bae, A. A. Gewirth, J. Gray, X. D. Zhu, T. P. Moffat, and W. Schwarzacher, Surf. Sci. **601**, 1886 (2007).

[28] J. Gray, W. Schwarzacher, M. K. O'Toole, and X. D. Zhu (unpublished).

[29] P. I. Cohen, G. S. Petrich, P. R. Pukite, G. I. Whaley, and A. S. Arrott, Surf. Sci. **216**, 222 (1989).

[30] J. Tersoff, A. W. Denier van der Gon, and R. M. Tromp, Phys. Rev. Lett. **72**, 266 (1994).

[31] X. D. Zhu, H. B. Lu, G. Z. Yang, Z. Y. Li, B. Y. Gu, and D. Z. Zhang, Phys. Rev. B **57**, 2514 (1998).

[32] X. D. Zhu, W. Si, X. X. Xi, and Q. D. Jiang, Appl. Phys. Lett. **78**, 460 (2001).

[33] H. Tanaka, T. Matsumoto, T. Kawai, and S. Kawai, Surf. Sci. **318**, 29 (1994).

[34] H. A. van der Vegt, H. M. van Pinxteren, M. Lohmeier, E. Vlieg, and J. M. C. Thornton, Phys. Rev. Lett. **68**, 3335 (1992).

[35] M. Zinke-Allmang, L. C. Feldman, and M. H. Grabow, Surf. Sci. Rep. **16**, 377 (1992).

[36] M. Born and W. Wolf, *Principles of Optics* (Pergamon, Oxford, 1993), p. 324.

[37] J. D. E. McIntyre and D. E. Aspnes, Surf. Sci. **24**, 417 (1971).